SANDIA REPORT
SAND2011-8778
Unlimited Release
Printed December 2011

Dynamic Reactor Modeling with Applications to SPR and ZEDNA

Ahti J. Suo-Anttila

Prepared by
Sandia National Laboratories
Albuquerque, New Mexico 87185 and Livermore, California 94550

Sandia National Laboratories is a multi-program laboratory managed and operated by Sandia Corporation, a wholly owned subsidiary of Lockheed Martin Corporation, for the U.S. Department of Energy's National Nuclear Security Administration under contract DE-AC04-94AL85000.

Issued by Sandia National Laboratories, operated for the United States Department of Energy by Sandia Corporation.

Available to DOE and DOE contractors from
U.S. Department of Energy
Office of Scientific and Technical Information
P.O. Box 62
Oak Ridge, TN 37831

Telephone: (865) 576-8401
Facsimile: (865) 576-5728
E-Mail: reports@adonis.osti.gov
Online ordering: http://www.osti.gov/bridge

Available to the public from
U.S. Department of Commerce
National Technical Information Service
5285 Port Royal Rd.
Springfield, VA 22161

Telephone: (800) 553-6847
Facsimile: (703) 605-6900
E-Mail: orders@ntis.fedworld.gov
Online order: http://www.ntis.gov/help/ordermethods.asp?loc=7-4-0#online

SAND2011-8778
Unlimited Release
Printed December 2011

Dynamic Reactor Modeling with Applications to SPR and ZEDNA

Ahti J. Suo-Anttila
Computational Engineering Analysis
Albuquerque, NM 87112

Abstract

A dynamic reactor model has been developed for pulse-type reactor applications. The model predicts reactor power, axial and radial fuel expansion, prompt and delayed neutron population, and prompt and delayed gamma population. All model predictions are made as a function of time. The model includes the reactivity effect of fuel expansion on a dynamic timescale as a feedback mechanism for reactor power. All inputs to the model are calculated from first principles, either directly by solving systems of equations, or indirectly from Monte Carlo N-Particle Transport Code (MCNP) derived results. The model does not include any empirical parameters that can be adjusted to match experimental data. Comparisons of model predictions to actual Sandia Pulse Reactor SPR-III pulses show very good agreement for a full range of pulse magnitudes. The model is also applied to Z-pinch externally driven neutron assembly (ZEDNA) type reactor designs to model both normal and off-normal ZEDNA operations.

Acknowledgments

The author wishes to acknowledge the contributions of Curtis Peters, who ran numerous MCNP calculations for deriving feedback coefficients for both SPR and ZEDNA type reactors. Ed Parma, who helped in formulating the dynamic reactor model and Pat Griffin, who helped to formulate the effects of prompt and delayed gammas on diagnostic detectors, such as photo-conductive diamonds (PCDs).

Contents

Figures

Tables

Nomenclature

EDNA	externally driven neutron assembly
FBR	fast burst reactors
FWHM	full width, half maximum
MCNP	Monte Carlo N-Particle Transport Code
PCD	photo-conductive diamond
SAR	safety analysis report
SNL	Sandia National Laboratory
SPR	Sandia Pulse Reactor
SPRF	Sandia Pulsed Reactor Facility
UTS	ultimate tensile strength
YS	yield strength
ZEDNA	Z-pinch externally driven neutron assembly

ρ_x	reactivity due to axial expansion, tabular from MCNP
ρ_{ri}	reactivity due to inner radius expansion, tabular from MCNP
ρ_{ro}	reactivity due to outer radius expansion, tabular from MCNP
ρ_{sb}	reactivity due to safety block motion, tabular from MCNP
Λ	neutron generation time = l/k_{eff} , where l is the neutron lifetime (s)
ρ	reactivity = $1 - 1/k_{eff}$, where k_{eff} is the effective multiplication factor
\$	reactivity in dollars = ρ/β
c	speed of sound
C_i	delayed neutron precursor inventory
C_p	heat capacity (J/g-°C)
E	Young's Modulus
k	the thermal conductivity (W/m-°C) of the fuel
P	reactor power (W) or neutron population,
Q_v	the reactor volumetric heat source (W/m^3)
r	radial coordinate
S	neutron source term (W/s)
T	reactor temperature (K or °C)
t	time (s)
T	reactor average temperature
T_0	initial reactor temperature
u_r	radial expansion subscripts o=outer, i=inner radius
v_x	axial expansion
x	motion of the safety block

σ	Poisson's ratio
α	thermal expansion coefficient
β	the delayed neutron fraction
λ_i	the delayed neutron precursor group decay constant
ρ	material density
ρ_f	the reactor fuel density (kg/m^3)

1 Introduction

There have been numerous computational models of Sandia Pulse Reactor (SPR) type fast burst reactors (FBRs) (Hetrick [1971], Reuscher [1969], Reuscher [1972], Burgreen [1962]). The models have been either thermo-mechanical or coupled neutronic thermo-mechanical. Reuscher (1969, 1972) developed several one- and two-dimensional thermo-mechanical models of SPR-type reactors (primarily SPR-II). He also reported the results from a coupled neutronic/thermo-mechanical model. Wright (2006) developed a MathCAD model of coupled point kinetics and one-dimensional elastic radial displacement equations. Miller (1994) calculated the three-dimensional fuel and structural vibrations of SPR-type reactors subjected to a variety of prescribed reactor power histories. Although all of these models were shown to work (i.e., reproduce the power history of the SPR-III reactor they were modeling), they all relied on some type of neutronic feedback coefficient that was measured experimentally or obtained empirically, or, in the case of Miller (1994), the reactor power history was specified as input, not calculated.

Most of these reactor models utilize some type of empirical parameters, such as reactivity feedback coefficients, that can be adjusted to obtain agreement between actual reactor data and the model predictions. However, when trying to predict the behavior of a reactor that is a design concept, many assumptions must be made as to the correct values for any adjustable parameters. In order to overcome this uncertainty, a dynamic reactor model has been developed that has no adjustable parameters. All feedback coefficients are derived by solving systems of equations, combined with feedback coefficients derived from Monte Carlo N-Particle Transport Code (MCNP) calculations. As such, the model can be applied to other reactor designs with increased confidence in its predictions, so long as the appropriate feedback coefficients have been derived from MCNP calculations of the same reactor.

A recent model by Wilson (2005) used a coupled approach, where the elastic expansion equations are solved and the expansion is coupled directly to MCNP at each time step. This approach is very similar to the one used here, except that MCNP is used at each time step, rather than in a separate stand alone mode. The approach works; however, there are issues with computational time, and with the smoothness of the computational results.

The reason that transient thermo-mechanical equations need to be solved for FBR and externally driven neutron assembly (EDNA) type reactors is that they have pulse widths on the order of 100 μs and less; thus very rapid heating of the reactor fuel occurs. Although the temperature rise follows the integral of the reactor power curve, the very rapid heating does not allow thermal expansion to occur simultaneously due to mass inertia. As a result, thermal expansion creates compression and expansion waves that propagate throughout the reactor fuel. Reuscher (1969) has solved the coupled thermo-elastic equations for transient expansion in selected one-dimensional geometries. The results of his calculations indicate that ringing of the reactor occurs at the fundamental frequencies, and the delay in thermal expansion causes the large power pulses in SPR type reactors. Thus modeling the expansion as a transient is essential to reproducing the reactor pulse behavior.

Although for EDNA type systems, the reactor is not driven super prompt critical, similar transient expansion will occur if the fuel is metallic plate type similar to SPR-III. For an EDNA device, the expansion is not required to terminate the pulse, provided the reactivity is less than $1.00. However, the dynamic behavior is important in understanding the performance

characteristics of the machine, in determining the radial and tangential stresses in the fuel, and in analyzing accident and abnormal conditions.

In this report, an approach similar to Reuscher's is taken in solving the coupled neutronic/thermo-elastic behavior of the reactor. The thermo-mechanical elastic expansion equations are solved and provide reactivity feedback to a coupled point-reactor kinetics model. The unique aspect of the solution presented in this work is that the feedback coefficient for reactivity as a function of fuel plate expansion and contraction is calculated separately from an MCNP model of the SPR-III reactor, rather than at each time step as in Wilson's model. In other words, the results presented are derived entirely from first principles, with no experimental input—other than for comparative purposes. The value of making such a first principles model is to demonstrate how close to experiment one can come by using existing tools and models, without resorting to modeling knobs (fudge factors) that can be adjusted to match the experimental measurements.

The motivation of this modeling effort is to apply this computational approach to EDNA devices using the SPR-III results as a validation of the model. The initial application will be for the Z-pinch externally driven neutron assembly (ZEDNA) reactor using 20% enriched fuel in a plate geometry similar to SPR-III. Because such a reactor does not yet exist, this model will allow predictions of reactor behavior under a variety of conditions.

1.1 Description of Sandia Pulse Reactor SPR-III

The SPR-III FBR is shown in Figure 1.1 without its shroud cover. The reactor is annular so that objects that need testing can be placed within the central cavity to allow exposure to the maximum neutron fluence possible. This report contains typical SPR-III operating characteristics (Section 4). These are also the characteristics that a replacement for SPR-III, such as ZEDNA, should strive to achieve. The properties of most interest are the pulse width and the total fast neutron fluence. For SPR-III, the pulse width at half maximum is 76 μs, and the total fluence in the pulse is 6.1×10^{14} n/cm^2. This is equivalent to a 1-MeV neutron fluence of 5.4×10^{14} n/cm^2, in terms of the radiation damage in silicon, when integrated over all energy bins in the neutron spectrum.

Figure 1.1 shows the metallic fuel plate stack at the top of the reactor. The lower core fuel plate stack is also shown but partially covered by the reflectors. The support bolts and rings which hold the fuel plate stacks together can also be seen. A simplified one-dimensional mechanical model of these supporting structures is included in the overall dynamic model.

1.2 Description of ZEDNA

The current ZEDNA reactor design is similar to the SPR-III reactor but different in size, geometry, and fuel material. An artist's depiction of this reactor is shown in Figure 1.2. The major design differences between SPR and ZEDNA consist of U10-Mo fuel enriched to 20% ^{235}U, larger size, height 62 cm, diameter 30.5 cm, and an inner movable fuel cylinder which comprises a safety block. The safety block has an outer diameter of 16 cm and an inner diameter of 11 cm. A 1-cm gap exists between the inner and outer fuel cylinders.

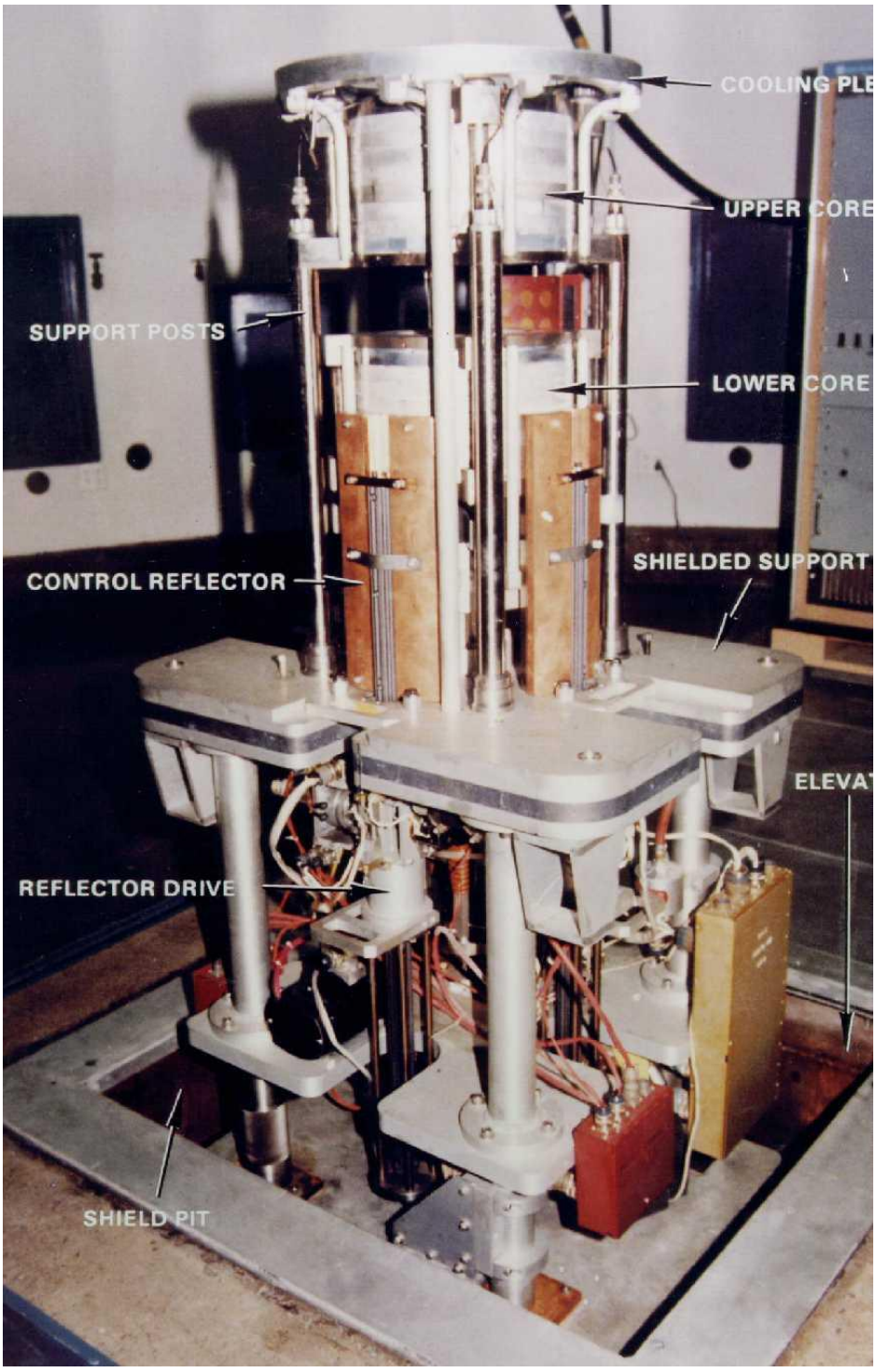

Figure 1.1. SPR-III Reactor at SNL

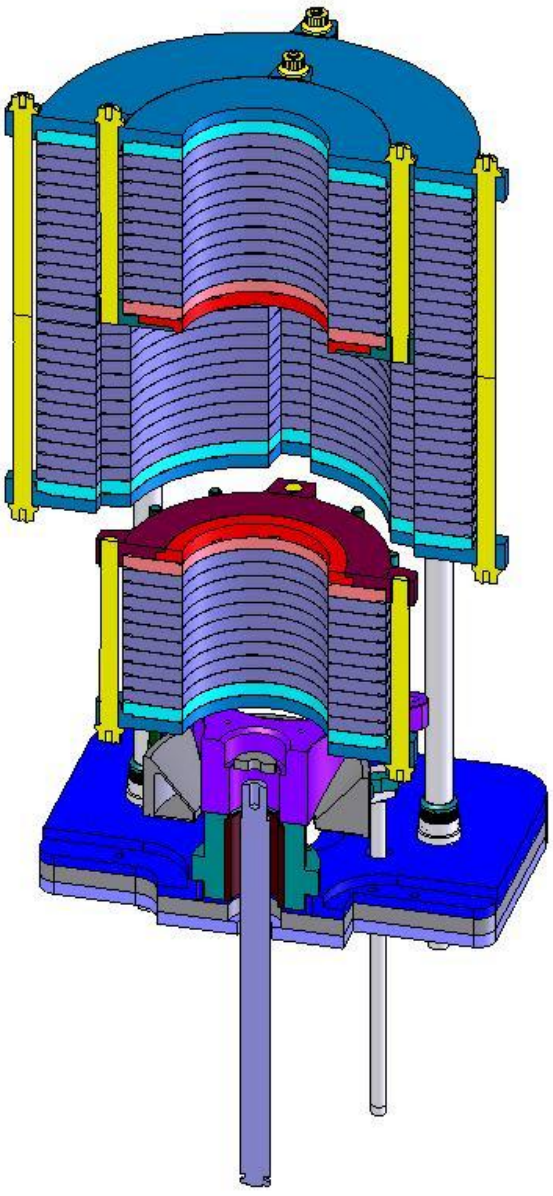

Figure 1.2. Current ZEDNA Reactor Design Showing the Divided Core which Operates as a Safety Block

2 Dynamic Reactor Modeling

The numerical model consists of simultaneously solving the point-reactor kinetics equations for reactor power, an energy equation for the reactor temperature, and transient elasticity equations for radial and axial expansion of the fuel. The expansion is combined with a reactivity feedback coefficient and power deposition profile derived from MCNP calculations. MCNP is used to create both the expansion feedback coefficients, and radial and axial temperature distributions. Together these equations describe the most important design aspects of the reactor, such as reactor performance characteristics and stresses in the fuel plates. Note that in this model, the MCNP calculations are uncoupled from the rest of the model. The MCNP results are embedded within the overall model as lookup tables of reactivity as a function of radial, axial, and safety block displacement.

In addition to the fundamental predictions of reactor power and fuel plate expansion, secondary computations provide details on prompt and delayed neutrons, prompt and delayed gamma, and transient fuel plate stress and strain.

This report presents a description of the model and case study results for the SPR-III reactor compared to experimental results. The work, to date, has been focused on determining if this type of modeling approach is adequate for FBRs and EDNA concepts. The results presented show that this simplistic approach, using one-dimensional analysis, and applying first principle reactivity feedback from separate MCNP calculations, is adequate for FBRs and EDNA type concepts.

3 Point-Reactor Kinetics Equations

The point-reactor kinetics equations have been used in numerous dynamic reactor models with success. The point-reactor kinetic equations can be derived from the neutron transport equations by making some simplifying assumptions such as a steady flux shape (fundamental mode) with time. The basic assumption is that the neutron population as a function of time can be described as zero-dimensional in space and energy. Prompt and delayed neutrons are accounted for using simple first-order rate equations that can be solved numerically as a function of time. The main variable is the reactivity, which can change as a function of time by insertion of control elements or by feedback from temperature or other drivers. Application of the point-reactor kinetic equations to ZEDNA type reactors violates the assumptions of the point kinetic derivation, because the governing equations are not homogeneous due to non-zero neutron source terms. Recently the point kinetic equations have been compared to exact numerical solutions for reactors with neutron sources and shown to have excellent agreement over a wide range of reactivity insertions (Eriksson, 2005). Since the neutron source duration occurs over a very short time span (less than 1μs), compared to the reactor decay time, a fundamental mode in the neutron population is reached well within 1 μs following the initial source injection and, therefore, the point-reactor kinetics equations will apply. Hence, the applicability of point kinetics to ZEDNA type reactors appears to have been confirmed.

The point reactor kinetics model solves the following equation for reactor power vs. time with a source.

$$\frac{dP(t)}{dt} = \frac{(\rho(t) - \beta)}{\Lambda} P(t) + S(t) + \sum \lambda_i C_i(t)$$

where

P	is reactor power (W) or neutron population,
t	is time (s),
ρ	is the reactivity = $1 - 1/k_{eff}$, where k_{eff} is the effective multiplication factor,
Λ	is the neutron generation time = l/k_{eff} , where l is the neutron lifetime (s),
β	is the delayed neutron fraction,
S	is the neutron source term (W/s),
λ_i	is the delayed neutron precursor group decay constant, and
C_i	is the delayed neutron precursor inventory.

The neutron lifetime l, can be obtained from the MCNP model of the reactor. The delayed neutron population is often modeled by splitting the population into six groups with various source terms and half-lives. The group parameters appear in Hetrick (1971). The equation governing the inventory of delayed neutrons for each group is

$$\frac{dC_i(t)}{dt} = \frac{\beta_i}{\Lambda} P(t) - \lambda_i C_i(t)$$

Although the power and precursor equations are solved in the model, it is really only the prompt neutrons that play a role in the pulse characteristics associated with an FBR or EDNA. However, when comparisons are made to experiment, the effect of delayed neutrons is significant when

examining the tail of the pulse, indeed as much as 30% of the energy in a pulse can be attributed to the tail.

A thermal energy equation for the reactor is

$$\rho_f C_p \frac{\partial T}{\partial t} = \nabla k \nabla T + Q_v$$

where

T	is the reactor temperature (K or °C),
t	is time (s),
C_p	is heat capacity (J/g-°C),
Q_v	is the reactor volumetric heat source (W/m^3),
ρ_f	is the reactor fuel density (kg/m^3), and
k	is the thermal conductivity (W/m-°C) of the fuel.

Effects such as heat losses to the environment are included through boundary conditions. However, heat losses and thermal conduction are negligible because the time scale of the reactor pulse is on the order of milliseconds, where heat transfer is negligible. Temperature gradients that are created due to the non-uniform fission distribution are included by interpolating normalized fission profile lookup tables derived from MCNP calculations. The lookup tables are imbedded in the heat source terms of the energy equation.

The reactivity feedback due to the effects of thermal expansion is governed by the following equation:

$$\rho = \frac{d\rho_d}{dT}(T - T_0) + \rho_{ro}(f(u_{ro})) + \rho_{ri}(f(u_{ri})) + \rho_x(f(v_x)) + \rho_{sb}(f(x))$$

where ρ is the net reactivity effect,

$\frac{d\rho_d}{dT}$	is the derivative of reactivity due to thermal effects such as Doppler, from MCNP—but not including thermal expansion.
$\rho_{ro}(f(u_{ro}))$	is the reactivity due to outer radius expansion, tabular from MCNP,
$\rho_{ri}(f(u_{ri}))$	is the reactivity due to inner radius expansion, tabular from MCNP,
$\rho_x(f(u_x))$	is the reactivity due to axial expansion, tabular from MCNP,
$\rho_{sb}(f(x))$	is the reactivity due to safety block motion, tabular from MCNP,
T	is the reactor average temperature,
T_0	is the initial reactor temperature,
u_r	is the radial expansion subscripts o=outer, i=inner radius,
v_x	is the axial expansion, and
x	is motion of the safety block.

A tabular set of reactivity feedback values, derived from MCNP calculations, is used in the model. The values can be interpolated for intermediate positions within the calculated values. The values could be changed into a functional form that could be used directly by the model if the form was known. Power law curve fits have been avoided because of very poor extrapolation capabilities. Extrapolations are required for some accident scenarios.

This set of equations is solved simultaneously by second-order accurate numerical methods. The model produces transient solutions of power, fuel displacement, and temperature, based upon initial conditions of reactivity, reactor temperature, and reactor power.

3.1 SPR-III MCNP Calculated Variable Radial and Axial Expansion

An MCNP model of the SPR-III reactor was used as a starting point to derive the displacement feedback coefficients for this model. The MCNP model was run in the kcode mode numerous times to create a set of data of reactivity versus reactor fuel expansion or contraction. Since the radial and axial expansion varies with time and position, a large set of calculations were performed to establish feedback coefficients for many possible expansions. The inner and outer radii expand and contract independently so each of the radii was allowed to expand and contract by varying degrees. In principle, the expansion and contraction for each fuel plate could have been calculated independently. However, because the speed of sound is uniform in the fuel matrix, and pulse timing is the same for all fuel plates, the vibration of all outer and inner radii is simultaneous. Therefore, in the MCNP model, the fuel plates were expanded simultaneously, but the amount of total expansion was proportional to local fission density in each fuel plate. This assumption is valid if the radial temperature distribution function is approximately the same in all the fuel plates (which is approximately true). Each expansion direction is calculated independently so that both radial and axial coefficients can be derived as partial derivatives. In the overall model, it is assumed that the reactivity feedback effects of both radial and axial expansion can be treated as partial derivatives and added to obtain a net reactivity for the point-reactor kinetics model.

The radial expansion reactivity feedback coefficients were derived based upon variable expansion of the core, i.e., an axial dependence of the radial expansion was assumed and made proportional to the local fission density. Table 3.1 lists the resulting normalized fission density for all 18 fuel plates. Plate number one is the top plate; plate number 18 is the bottom plate. This normalized value was multiplied by the input expansion value to give a local fuel plate expansion for the MCNP calculation. Feedback coefficients for normalized expansion were generated in this way.

Table 3.1. Normalized Axial Fission Density as a Function of Fuel Plate

Plate	Multiplier
1	0.44
2	0.61
3	0.75
4	0.87
5	0.96
6	1.04
7	1.09
8	1.1
9	1.26
10	1.31
11	1.21
12	1.28
13	1.3
14	1.28
15	1.21
16	1.09
17	0.93
18	0.7

Note that the axial fission density is not symmetric about the centerline (between plates 9 and 10). This is due to the construction of the SPR-III reactor and the reflector elements being inserted from below the reactor. The MCNP calculations expanded the core axially at both ends simultaneously to obtain the axial reactivity feedback coefficients. However, due to the asymmetry, equal and opposite axial expansion will not occur. This effect was not taken into account in the MCNP calculations because axial feedback is not as strong as radial feedback; hence the additional detail would have a small effect on the predicted results. Additionally, such a calculation would require iterations between expansion predictions from this model and MCNP calculations. In the results that follow, only half the core is modeled for predicting axial expansion, and the reactivity effect is assumed the same for both halves.

The normalized radial power density is shown in Table 3.2. The radial power density varies slightly from one plate to the next, but the variation is small. Therefore, a normalized average power density is used in the model which represents an average of all 18 fuel plates.

Table 3.2. Normalized Average Radial Power Density in the SPR-III Reactor

(R-Ri) (Ro-Ri)	Multiplier
0.1	1.147
0.2	1.191
0.3	1.201
0.4	1.172
0.5	1.131
0.6	1.063
0.7	0.979
0.8	0.878
0.9	0.766
1	0.623

Three tables of expansion feedback coefficients were generated from the MCNP runs. Table 3.3 expands only the outer radius, Table 3.4 expands only the inner, and Table 3.5 expands only in the axial direction.

Table 3.3. MCNP Reactivity Feedback Coefficients for Outer Radius Expansion

Outer Radius (cm)	Expansion (cm)	k_{eff}	δK	$\delta\rho$ ($)
14.859	0.00	1.00897	0	0.0
14.869	0.01	1.00859	-0.00038	-0.058
14.879	0.02	1.00820	-0.00077	-0.118
14.899	0.04	1.00749	-0.00148	-0.228
14.919	0.06	1.00694	-0.00203	-0.312
14.939	0.08	1.00625	-0.00272	-0.418

Table 3.4. MCNP Reactivity Feedback Coefficients for Inner Radius Expansion

Inner Radius (cm)	Expansion (cm)	k_{eff}	δK	$\delta\rho$ ($)
8.87	-0.01	1.00896	-1E-05	0.002
8.88	0.00	1.00897	0	0.0
8.89	0.01	1.00893	-4E-05	-0.006
8.90	0.02	1.00891	-6E-05	-0.009
8.91	0.03	1.00868	-0.00029	-0.045
8.92	0.04	1.00869	-0.00028	-0.043

Table 3.5. MCNP Reactivity Feedback Coefficients for Axial Expansion.

Expansion – cm	k_{eff}	δK	$\delta\rho$ ($)
0.0	1.00245	0	0.0
0.04	1.00205	-0.0004	-0.062
0.08	1.00147	-0.00098	-0.151
0.12	1.00086	-0.00159	-0.245
0.16	1.00016	-0.00229	-0.352

Table 3.6 is a compilation of the MCNP results for safety block motion. The safety block will drop during large pulses and will be electrically activated during small pulses. Large pulses will give the safety block a sufficient kick to separate the magnetically coupled sections of the core. Small pulses do not have sufficient expansion to separate the core, and rely upon termination of power to the electromagnet for separation.

Table 3.6. MCNP Reactivity Feedback Coefficients for Safety Block Motion

Distance – cm	k_{eff}	δ k	δ Reactivity $
0.0	1.00897	0	0
.5	1.00160	-0.00737	-1.133846
1.0	0.99554	-0.01343	-2.066154
1.5	0.99028	-0.01869	-2.875385
2.0	0.98535	-0.02362	-3.633846
2.5	0.98113	-0.02784	-4.283077

The tabular results were implemented into the overall model as numerical lookup tables with intermediate values derived by piecewise linear interpolation. Values outside the table were linearly extrapolated from the nearest values in the tables.

3.2 Elastic Expansion and Contraction Equations

The elastic expansion and contraction equations were taken from Reuscher. The displacement in the radial direction is governed by the following equation:

$$\frac{\partial^2 u}{\partial r^2}+\frac{1}{r}\frac{\partial u}{\partial r}-\frac{u}{r^2}-\frac{(1+\sigma)}{(1-\sigma)}\alpha\frac{\partial T}{\partial r}-\frac{1}{c^2}\frac{\partial^2 u}{\partial t^2}=0$$

where

u = u(r,t) is the radial displacement
r = radial coordinate
t = time coordinate
c = speed of sound, $E(1-\sigma) / [(1+\sigma)(1-2\sigma)\rho_m]$
σ = Poisson's ratio
E = Young's Modulus
ρ_m = material density
α = thermal expansion coefficient
T = T(r,t) is the temperature change

Note that only the temperature gradient appears in the elastic wave equation. This implies that uniform heating will not create thermal expansion waves within the interior of the medium; instead the waves are created at the boundaries, via the boundary conditions.

The fuel plates in the radial direction are unconstrained so that the radial boundary conditions are zero radial stress at the inner and outer boundaries

$$Stress=(2\mu+\lambda)\frac{\partial u}{\partial r}+\frac{\lambda u}{r}-(3\lambda+2\mu)\alpha T(r,t)=0$$

where

$\mu = E / (2(1+\sigma)]$
$\lambda = \sigma E / [(1+\sigma)(1-2\sigma)]$

If the reactor is split radially into sliding sections, as ZEDNA may be, then zero radial stress is applied at the gap location as well as the inner and outer boundaries of the fuel. In this way, only a single equation is solved for radial displacement, even though different sections of the radial displacement may be uncoupled from one another.

The axial displacement equation is treated independent of the radial displacement because the fuel plates are touching only on the outer ring (approximately 1-cm thick). Hence, there are only small gradients of displacement in the orthogonal direction. Thus, the displacement coupling (via Poisson's ratio) between the two directions is relatively weak and, therefore, ignored for simplicity.

The axial displacement wave equation is

$$\frac{1}{A}\frac{\partial}{\partial x}(2\mu+\lambda)A\frac{\partial v}{\partial x}-(3\lambda+2\mu)\alpha\frac{\partial T}{\partial x}-\rho\frac{\partial^2 v}{\partial t^2}=0$$

where

v = v(x,t) is the axial displacement
x = axial coordinate
T = T(x,t) is the axial temperature change
A = cross-sectional area

The axial boundary condition is significantly more complicated. In the SPR-III reactor, the fuel plates are clamped by steel rings held together by eight Inconel bolts, each 1-inch in diameter. Thus, there exists a significant compressive axial stress within the fuel plate outer edges at all times. Only the outer 1 cm of the fuel plate makes contact with the other fuel plates, and the remainder of the fuel plate axial area is separated by a small gap, hence that portion of the fuel plate is axially stress free. The unconstrained portion of the fuel plate will fill the pre-existing gaps when it expands axially, but this effect is assumed to have no reactivity feedback. However, the whole plate is displaced axially by that portion of the fuel plate which is in contact with the other plates. This axial displacement does have a reactivity feedback. To simplify this analysis, the true axial reactivity is assumed to be somewhere between the limits of zero and 100% of the MCNP calculated axial reactivity effects. In some calculations both limits will be shown, in others only one limit is chosen.

In order to simulate the effect of translating axial fuel in the gap region, the density of the fuel is increased by a scale factor that is equal to the area ratio of all the fuel to the area of the fuel which is in contact. When the outermost fuel ring that is in contact moves, it drags along the rest of the fuel plate. The inertial mass of the remaining (no contact) fuel plate is mimicked by increased fuel density in this one-dimensional model. Clearly a two-dimensional model is needed to do this more accurately, wherein the fuel in the gap zone would bend as well as translate during the reactor pulse. Such two-dimensional effects are superfluous because the current MCNP model is not capable of including such effects.

Reuscher used a mass-spring type boundary condition at the upper and lower fuel plate boundaries. In contrast, more realistic boundary conditions are obtained when the U-10Mo fuel, the steel clamps, and two halves of the Inconel bolts are included in the axial displacement equation by using variable properties, variable area, and fixed displacement boundary conditions.

Axial reactivity feedback is calculated from displacement of the outermost fuel plate rather than the outermost boundary (which never moves). The fixed axial displacement boundary conditions arise from symmetry at the Inconel bolt mid-plane and the initial bolt stress.

The initial axial displacement is found by solving the stress equation with the applied bolt stress

$$BoltStress = (2\mu + \lambda)\frac{\partial u}{\partial x} - (3\lambda + 2\mu)\alpha T(x,t)$$

Although the bolts are in tension rather than compression, the combination of reversal of direction and the symmetric nature of the elastic displacement equations results in the same set of equations from a mathematical standpoint. Hence, only the interpretation of the displacement, and its derivative (i.e., stress) changes.

After solving for the initial boundary displacement at the bolt mid-plane, the v_i values are held fixed for the duration of the transient calculation.

There exists one complication in this one-dimensional axial expansion formulation. That is, the effect of the steel rings which clamp the fuel plates together. Since the outer edge of the fuel plates does not align with the Inconel bolts, three-dimensional geometric leverage effects occur. The effect of the leverage is to reduce the bolt stress because the steel ring can flex laterally in three dimensions and absorb some of the fuel expansion, thereby reducing the tension on the bolts. This effect is not negligible because a comparison of the peak bolt stress calculated by this one-dimensional model to a three-dimensional finite element model (which includes the geometric details of the steel clamping rings and bolts) reveals that the one-dimensional approximation overestimates the bolt stress by a factor of 1.75. In order to approximate the effect of the steel clamping rings, the steel ring nodes utilize a reduced modulus of elasticity. A reduction of the steel ring modulus of elasticity allows the material to flex more, thereby absorbing more of the fuel plate axial expansion without passing the axial stress along to the Inconel bolts. In the current model, the degree of elasticity reduction in the steel rings was adjusted so that the one-dimensional and three-dimensional bolt stress predictions were identical. Although this seems artificial, the reduction in elasticity is still based upon a three-dimensional finite element computation (JAC3D code)—not fine-tuning to experimental measurements. Lastly, the overall effect upon reactor performance is very little. The unadjusted one-dimensional model could be used for all the results reported herein, and the primary differences are the axial stresses in the fuel plates and bolts. The reactor power and energy yield are reduced by 1.6% compared to the unadjusted model.

3.3 Summary of Computational Method

The computational method in this model is as follows:

1. Calculate radial and axial feedback coefficients from MCNP for various expansions. These feedback coefficients are hardwired into the model through lookup tables.
2. Assign geometric dimensions, material properties, reactor temperature, initial reactor power, and initial reactivity.
3. Calculate initial bolt stress, and use the resulting displacement as initial conditions for axial expansion equations. Initial radial expansion is zero stress and displacement.

4. Increment time by a small quantity (~0.01 to 1 μs), and update all dependent variables.
5. Interpolate reactivity tables for current reactivity feedback based upon radial and axial expansion.
6. Evaluate reactivity contribution due to reflector or safety block motion (if any).
7. Solve point-reactor kinetics for reactor power.
8. Solve energy equation for reactor temperature.
9. Solve radial expansion equations for radial displacement.
10. Solve axial expansion equations for axial expansion.
11. Go back to step 4 and repeat until calculation is completed.

4 SPR-III Calculation

The applicability and accuracy of the model is presented by comparing results to actual SPR-III operations. The first section will demonstrate how inertially delayed expansion of the fuel plates affects the reactivity and power. The next section will test the accuracy of the model by making detailed comparisons of two SPR-III pulses, one at high and the other at low energy yield. Detailed comparisons will include actual reactor power histories and total energy yield. Finally, a third comparison is made to various SPR-III maximum pulse data that has been previously published in Sandia National Laboratory (SNL) reports.

4.1 Coupled Neutronics-Temperature-Expansion of the SPR-III Reactor

The SPR-III reactor behavior can be explained by comparing the power curves of three test cases shown in Figure 4.1. The first test case shows the power level without any feedback, the second for instantaneous expansion feedback, and the third for delayed expansion feedback due to inertial ringing.

There is a considerable variation in power profile and level depending upon timing of the feedback. No feedback curve has unlimited power because the initial reactivity is above \$1.00. The power increases to infinity with the time constant $T = \Lambda/(\rho-\beta)$. For a reactivity addition of \$1.12, the reactor period is ~20 μs. The instantaneous expansion feedback case represents the condition if the fuel expanded instantaneously with temperature and with no inertial effects. Instantaneous feedback limits the power to a low value because the expansion of the core adds significant amount of negative feedback. The delayed feedback allows a higher power level to be reached than for the instantaneous case. The departure of the power curve from no-feedback case appears when feedback from fuel expansion begins to take effect. The effect of delayed expansion is readily apparent because the reactor can reach a significantly higher power level before thermal expansion can reverse the power excursion.

The properties of the SPR-III reactor are shown in Table 4.1. These properties were used in the simulation for the SPR-III model.

Table 4.1. Properties Used to Simulate the SPR-III Reactor Performance

Inner radius	8.8 cm
Outer radius	14.86 cm
Height	33 cm
Reactor mass	234 kg
Delayed neutron fraction	0.0065
Neutron lifetime	Pulse dependent, see text
Initial reactivity	Set by reactor operations
Normalized power axial	See Table 3.1
Normalized power radial	See Table 3.2
Reactivity feedback	See Table 3.3, Table 3.4,and Table 3.5

Safety Block reactivity	See Table 3.6
Initial power	0.001 Watt
Fuel density	17200 kg/m^3
Fuel specific heat	133 J/kg K
Fuel modulus of elasticity	f(temp) see text
Fuel thermal expansion coefficient	1.28e-5 m/m-C
Fuel Poisson's ratio	0.37
Fuel thermal conductivity	50 W/m-K
Inconel density	8220 kg/m^3
Inconel modulus of elasticity	29.4e6 PSI
Inconel Poisson's ratio	0.289
Steel density	7600 kg/m^3
Steel modulus of elasticity	27e6 PSI
Steel Poisson's ratio	0.31

The peak of the power profile occurs for the instantaneous and the delayed expansion cases when the negative reactivity feedback is such that there is exactly \$1.00 of reactivity in the core. The core is now prompt critical and no longer super prompt critical. Continued addition of negative reactivity brings the system reactivity below \$1.00 and the core becomes sub-prompt critical. It is the timing of the delayed expansion that determines the maximum power level reached. Reactors with fuel material that have slow sound speeds will delay the expansion for greater lengths of time, allowing higher power levels before being shut down. It is the complex interplay of the delayed thermal expansion, which is mass inertia and material elasticity dominated, and the reactivity expansion feedback effects that determines the reactor pulse power level and energy yield.

The reactivity state associated with the three cases (no feedback, instantaneous feedback, and delayed expansion feedback) is shown in Figure 4.2 and Figure 4.3 on an expanded time scale. There is basically no reactivity feedback until 0.5 ms because the fuel has not experienced a sufficient energy deposition to heat the core. The instantaneous feedback curve levels off at approximately \$0.88 of reactivity. The delayed feedback curve shows oscillations due to radial and axial expansion/compression waves. It is of greater magnitude than the instantaneous feedback curve due to higher power levels achieved, which corresponds to both higher temperatures and greater thermal expansion.

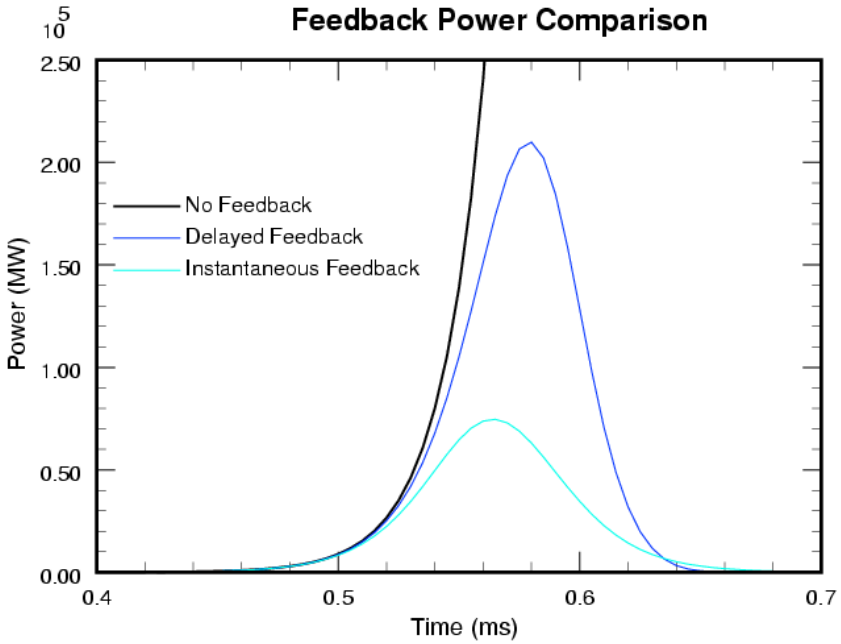

Figure 4.1. Calculated SPR-III Power History for the Cases of No Feedback, Instantaneous Feedback, and Delayed Expansion Feedback

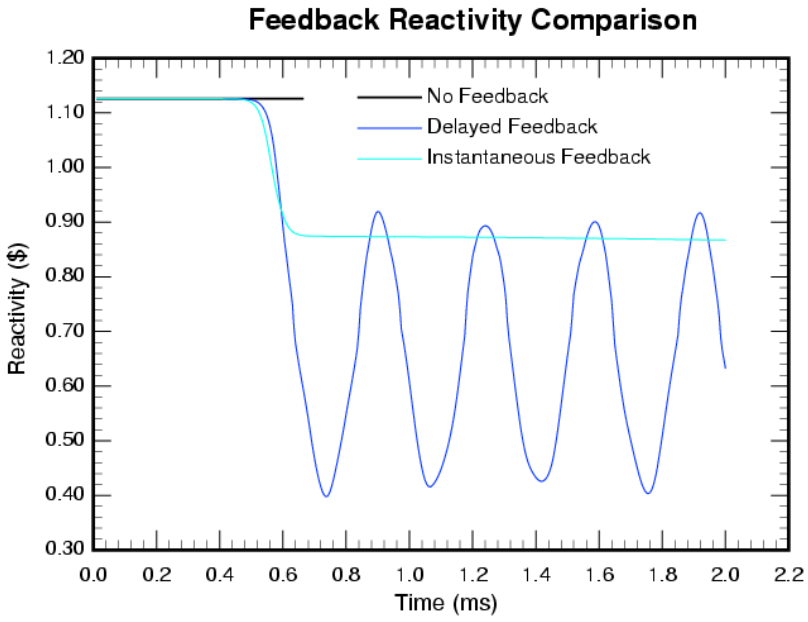

Figure 4.2. Calculated SPR-III Reactivity History for the Cases of No Feedback, Instantaneous Feedback, and Delayed Expansion Feedback

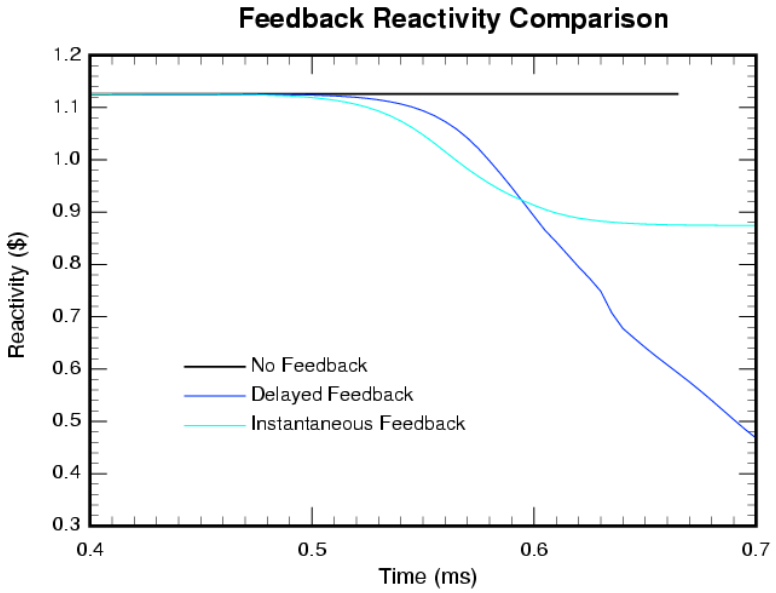

Figure 4.3. Calculated Reactivity History on an Expanded Time Scale

Also quite apparent in the delayed expansion curve is the amount of delay before reactivity is added as compared to the instantaneous case. It is estimated that the inertial effects cause approximately 50 to 75 μs delay in reactivity feedback.

4.2 Comparison to Measurements – Large 6.6 MJ SPR-III Pulse

Photo-conductive diamond (PCD) data was available for a 6.6-MJ pulse, which is approximately half the maximum pulse that the SPR-III can deliver. Figure 4.4 and Figure 4.5 show the power and energy trace for the actual pulse as compared to the model results.

In Figure 4.4 the red curve is the measured PCD curve, and the black curve is the model prediction. The PCD curve is not the raw voltage trace, rather it has been modified to account for prompt and delayed gamma radiation effects and represents the best estimate of actual reactor power. There are three distinct regions in the power trace. The first region is the actual high power pulse, the second region is the delayed neutron plateau, and the last region is the exponential power decay after the bump at approximately 0.1 seconds. The delayed neutron plateau is where the reactivity is less than zero and the reactor is multiplying delayed neutrons. The bump at 0.1 seconds is where the safety block hits bottom, stops moving, and terminating negative reactivity addition. After the safety block stops, the reactivity is fixed at a large negative value, and delayed neutron multiplication continues with exponentially decreasing power level.

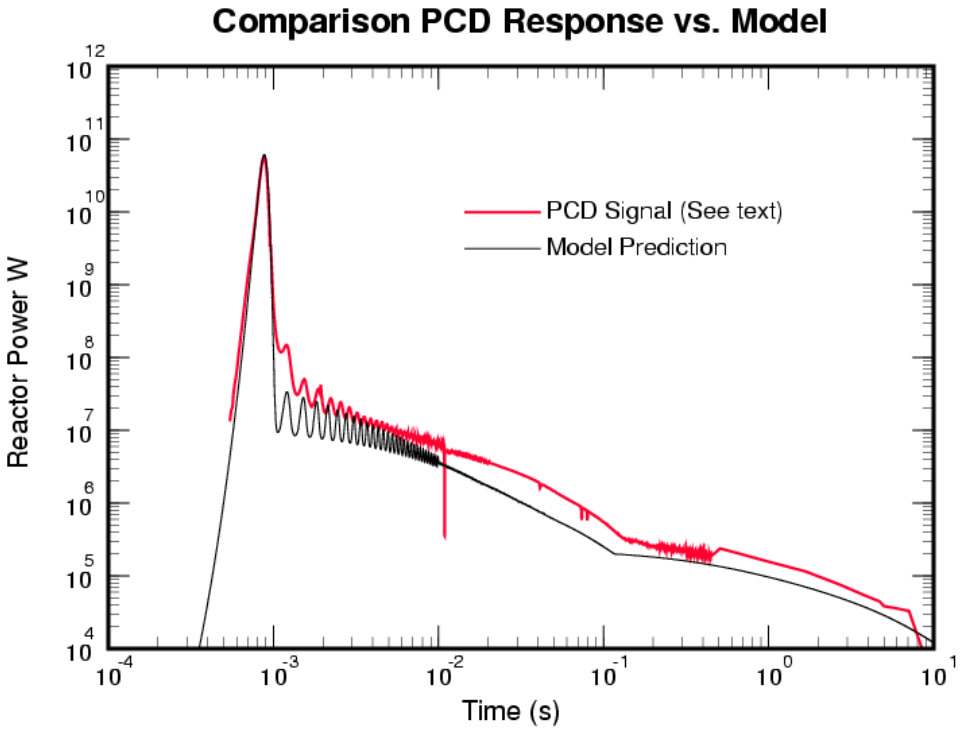

Figure 4.4. Measured and Calculated Reactor Power for a Large SPR-III Pulse (6.6MJ)

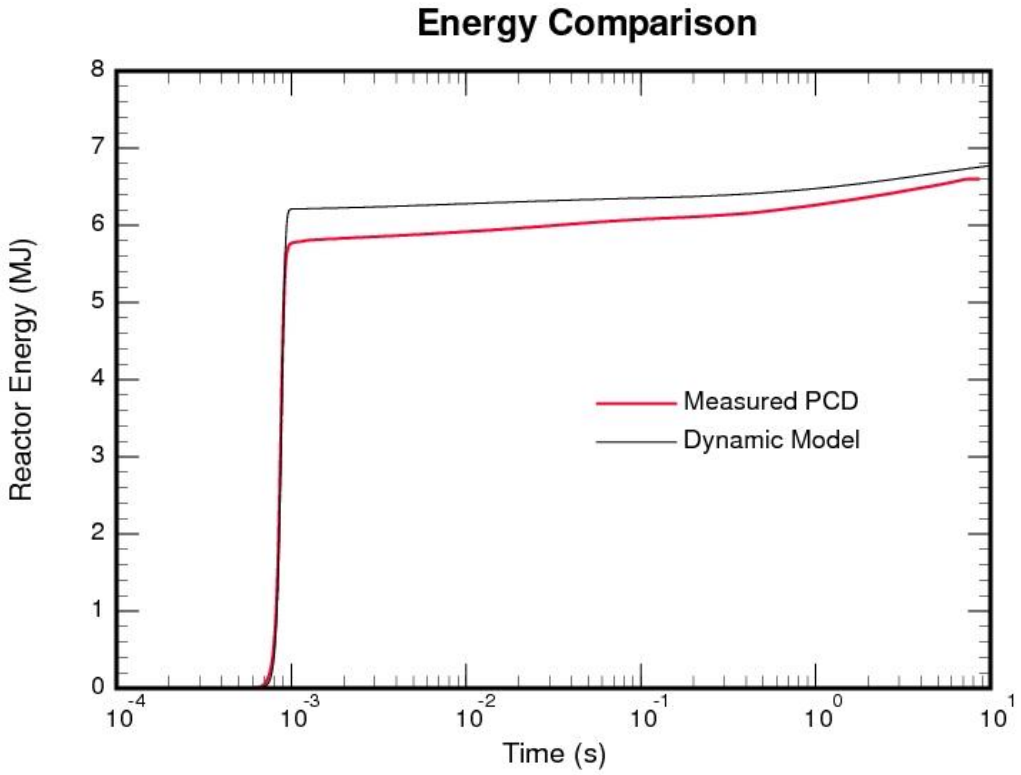

Figure 4.5. Measured and Calculated Energy Yield for a Large SPR-III Pulse (6.6 MJ)

The total energy yield is inferred by measuring the temperature rise from a thermocouple on the B plate near the reactor center. The thermocouple is located near the maximum temperature of this plate (approximately 1 cm beyond the inner radius). The maximum temperature rise is recorded at approximately 18 seconds after the pulse and is multiplied by the conversion factor 0.0222 MJ/°C to yield the total energy of the pulse. The source of the conversion factor is from the SPR-III reactor operators, and accuracy of this conversion is unknown.

One metric SPR-III operators use to determine the actual reactivity insertion in a shot is to measure the reactor period prior to the reactivity feedback effects. The initial reactivity is derived from the initial slope of the power trace

$$\frac{1}{P}\frac{dP}{dt} = \frac{(\rho - \beta)}{\Lambda}$$

Using a neutron lifetime 18.5 nanoseconds, the initial reactivity insertion for this pulse was derived to be \$1.0903. This was the initial reactivity insertion for the model calculation.

The model predictions shown in Figure 4.4 and Figure 4.5 are related to the timing and motion of safety block drop. The safety block is held in place by electromagnets during the pulse. As the reactor heats and expands, the rapid expansion is sufficient to break the magnetic coupling during the pulse and allows the lower half of the core (safety block) to drop. Dropping the safety block adds negative reactivity. The rate of negative reactivity addition is governed by the position of the safety block according to the reactivity data in Table 3.6. The position of the safety block is governed by several effects. First there is the initial kick due to fuel expansion; this gives the safety block some initial velocity. Next, there are compressed springs and gravity that accelerate, and magnetic effects which decelerate the safety block. All of these effects are present at the moment magnetic coupling is broken. It is not possible to know the precise magnitude of any of these effects other than gravity. In addition, the magnetic coupling and compression springs are located a significant distance from the location where the two core halves are in contact. Hence monitoring the compression force at the contact fuel point is only an approximate indicator of the force history at the electromagnetic coupling point. Dynamic time delays due to propagation of the elastic waves through the structural members that hold the core and its supports probably affect the exact timing of the core separation. Including such detailed effects is well beyond the current capabilities of this model.

The initial safety block velocity is estimated from the axial force integrated over the time of initial expansion (i.e., the impulse) and equating that to the initial momentum of the lower core half. The absorption of momentum by the electromagnets is assumed to be some fraction of the initial momentum. The axial force is estimated by applying an internal boundary condition of zero net displacement difference from the initial displacement (due to bolt stress) during the pulse. This zero displacement internal boundary condition is removed at the moment the safety block separates. During the computation, the axial force is monitored until its first peak. The first peak is the turnaround point where the axial expansion turns into contraction, and it is assumed to be the moment where the two core halves split from one another. Since the total time

integrated force is known, the initial velocity is estimated by dividing that linear impulse by the mass of the half core. The half core mass is estimated to be the weight of the fuel plus 25 kg of support and control structures.

One uncertainty is the effect of the electromagnets. Since these magnets are active during the pulse, they will absorb some of the linear impulse created by core expansion. It is known that the magnets will not release in a small 2-MJ pulse but will release in a 6-MJ pulse. Hence, a crude estimation is that half the linear impulse is absorbed by the electromagnets. The uncertainty introduced electromagnet impulse absorption amounts to about 0.2 MJ in total pulse yield. The calculated initial velocities are 0.4 m/s without impulse absorption and 0.2 m/s with one-half impulse absorption by the electromagnets. After the core splits, the internal boundary condition is removed from the calculation and the expansion and contraction waves are allowed to propagate freely in the core halves

Finally, the maximum free fall of the safety block is limited to 9 cm, with a slowdown before 9 cm due to a shock absorber. How the shock absorber affects the motion is not known because those details were not available. As a result, the shock absorber effects are ignored and the falling core is brought to a halt in a single time step.

The modeling parameters described above were made in order to estimate the behavior of the reactor, without resorting to fine-tuning adjustments. What is notable is that all of these estimations were calculated directly or indirectly by the model; there were no ad hoc estimations. What is also significant is that effects that were thought to be negligible have some effect upon that calculated energy, i.e., the linear impulse absorbed by the electromagnets. The effect is not huge, 0.2 MJ out of 7 MJ but noticeable nevertheless.

4.3 PCD Normalization and Scaling

Figure 4.4 includes a plot of the corrected PCD voltage normalized to the total reactor energy. How the raw PCD voltage relates to reactor power must be treated with some care because the diamond responds to both gamma rays and neutrons. In a reactor there are both prompt and delayed gammas. The prompt gammas can be scaled directly to reactor power. Each fission event yields approximately 175.6 MeV of thermal energy deposited locally by the fission fragments. There is additional energy in the form of gammas, prompt neutrons, and neutrinos. These other forms of energy are assumed to leave the reactor core and are not converted to local sensible heat. Beta decay is approximately local but is a small contributor and therefore ignored in this development. Thus the total number of fissions per second can be calculated by dividing the power level by 175.6 MeV times a conversion factor (1.602e-13 MeV/J). The prompt gamma power level (MeV/sec) is equal to 6.6 MeV/fission times the number of fissions/sec. Similarly the prompt neutron power level is 4.91 MeV/fission times the number of fissions per second.

Delayed gamma rays are more difficult to calculate. They are similar to delayed neutrons but are characterized by a complex function of time rather than a sum of simple half-lives. A plot of gamma power in MeV/sec per fission event is shown in Figure 4.6.

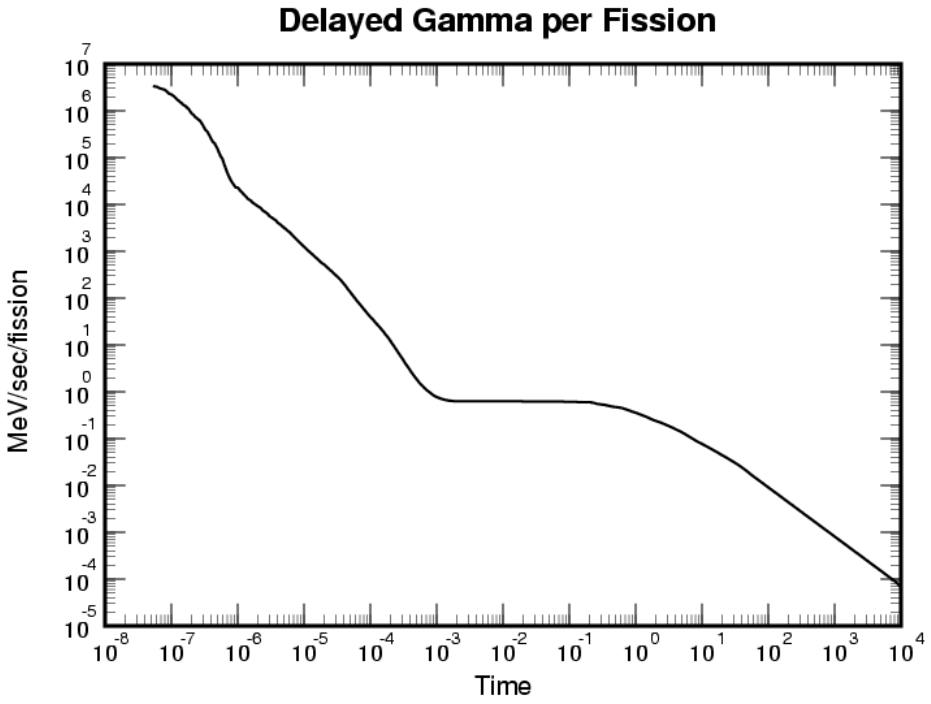

Figure 4.6. Delayed Gamma Energy Production as a Function of Time from a Fission Event

The accepted value for the total energy attributed to all gammas from a single fission event is 6.6 MeV. However, if the curve (in Figure 4.6) is integrated over time, a plot of the resulting integral is shown in Figure 4.7.

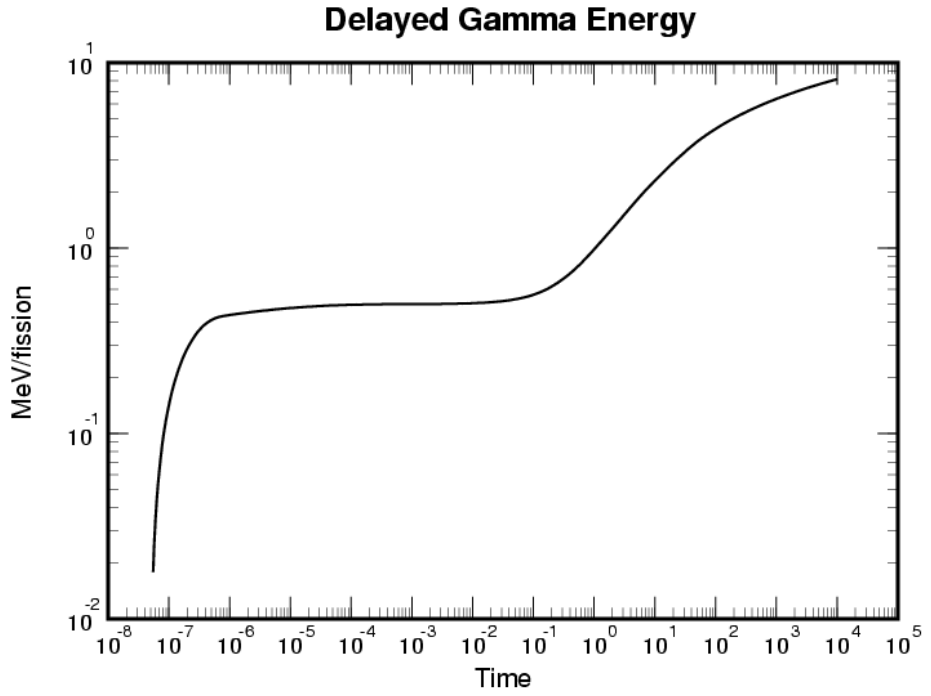

Figure 4.7. Total Energy Resulting from the Time Integral of the Data in Figure 4.6

As shown in Figure 4.7, the time integral of delayed gamma energy seems to approach 10 MeV per fission (using an eyeball extrapolation). Since the total time integral is reported by other investigators as 6.33 MeV, there is clearly an issue with the scale of the delayed gamma data. There exists some uncertainty with respect to the temporal emission of delayed gamma, primarily the late time gamma. Efforts are underway to resolve any discrepancies from the various sources of data. At present, the location and magnitude slight discrepancy cannot be determined since the data in Figure 4.6 is a composite of several different investigators. The current approach is to re-normalize the entire time dependent curve (Figure 4.6) by the ratio 6.33/8.1 = 0.78 which will force the integral to be equal to 6.33 MeV at the last data point, 10^4 seconds. This correction is temporary and will be replaced with a fully self-consistent gamma rate curve when the small data discrepancies are fully resolved.

The manner in which the delayed gamma power is calculated is as follows. First, the reactor power history is calculated. Next, the power history is converted to a number of fissions for each time step. Then for each power time step, time is marched backwards and a sum is created of the contribution of all the previous fissions weighted by the function shown in Figure 4.6 and the normalization factor 6.33/8.1. This backward time convolution integral yields the current time step gamma power level. Figure 4.8 shows a plot of prompt gamma, delayed gamma, and prompt neutron power as a function of time for a 6.6-MJ SPR pulse. From this figure it is clear that delayed gammas will dominate the PCD signal at about the time the safety block comes to rest (0.1 seconds).

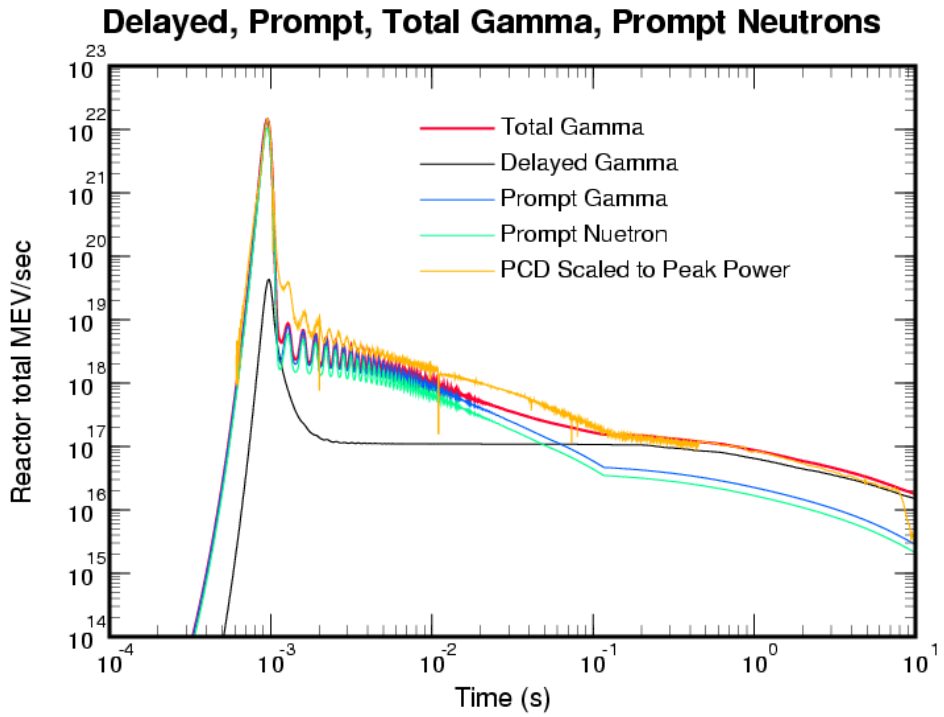

Figure 4.8. Power Level per Fission of Prompt Gamma, Delayed Gamma, Prompt + Delayed, and Prompt Neutrons as a Function of Time for a 6.5-MJ SPR Pulse

The weighting factors for how PCD voltage depends upon gammas vs. neutrons has some uncertainty associated with it. A series of MCNP calculations which predict the total dose

in the PCD were made. Subsequently, NJOY calculations were made to resolve to ionizing dose into its gamma and neutron components. These calculations include the gamma and neutron absorption effects of the reactor fuel prior to deposition in the PCD that was located outside the reactor by applying these dose efficiency factors and the absorption cross-sections of carbon yields an estimate of the total ionization in the carbon matrix due to both gamma and neutrons. By assuming that PCD electrical response is proportional to total carbon ionization rate, the reactor power history can be extracted from the PCD signal by an iterative process. During the iterative process, the predicted power level is normalized to the total energy of the pulse. Although this process has some uncertainty, it is the current best estimate for the reactor power from a PCD signal. In addition to computational uncertainty, there is also experimental uncertainty in the PCD signal. In spite of all the sources of uncertainty, the level of agreement between the predicted and measured power during and after the pulse is considered quite good.

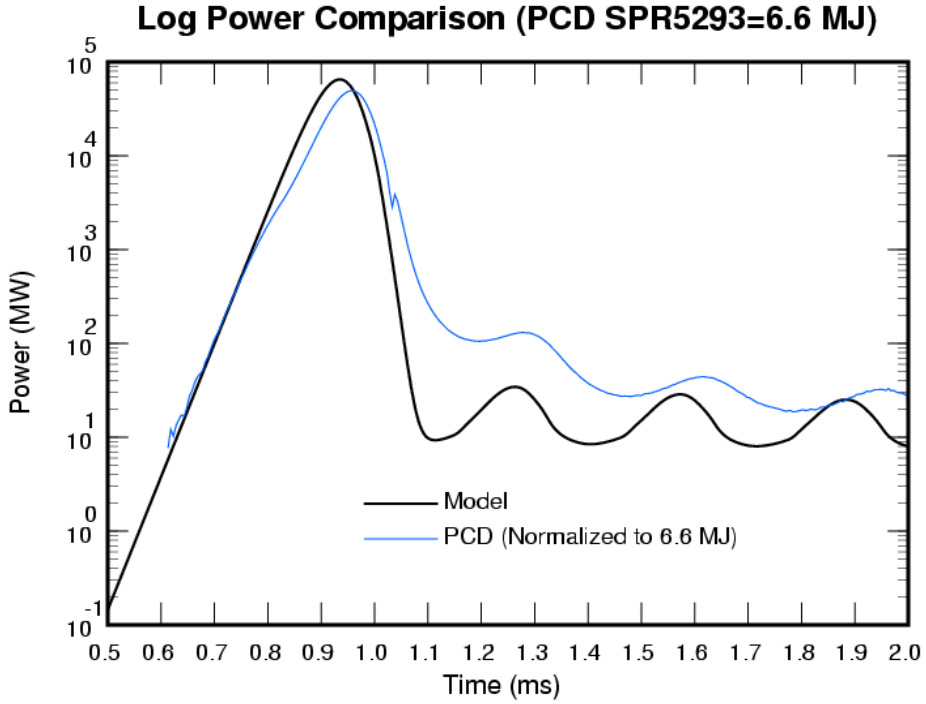

Figure 4.9. Detail of Power vs. Time for the 6.6 MJ Pulse

In Figure 4.4 and Figure 4.8, some details of the measurements are discussed. First, there were two PCDs in the reactor pulse, and the data in this report is a composite of the best data from both PCDs rather than a single one. Both PCDs were subject to significant amounts of noise; therefore, to reduce the noise, a composite curve of the best data from both PCDs was created and used. Ideally, the curves would have overlaid exactly, but glitches in the blue (Figure 4.8) and red (Figure 4.4) curves are the points where the two curves were joined. The magnitude of the glitches gives the reader some idea of the reproducibility of the data from a PCD.

Another effect shown in Figure 4.9 is the ringing of the reactor. The power pulsations in the tail of the pulse are due to reactivity variations caused by the radial expansion and contraction of the fuel plates. As can be seen, the vibration period is close but not exact.

The mismatch is probably a two-dimensional effect, as noted by Reuscher, wherein a two-dimensional elasticity calculation vibrates at a slightly lower frequency, compared to a one-dimensional vibration.

4.4 Comparison to Measurements – Small 1.88 MJ SPR-III Pulse

Detailed reactor PCD data was available for a small 1.88-MJ pulse. The small reactor pulse was predicted to have a longer neutron lifetime, approximately 23.5 ns, (versus the 18.5 ns for the larger 6.6-MJ pulse) using MCNP with extended lifetimes for neutron tracking. The longer neutron lifetime is attributed to reflections from the building and ground. The initial reactivity reported by the operators was based upon 18.5-ns lifetime and is created by hardware curve fits to the initial power trace. If the neutron lifetime is longer, a correction needs to be made to the initial reactivity insertion.

The reported reactivity \$1.0122 was corrected by the equation above to a values of \$1.0225 due to the longer predicted neutron lifetime. The corrected reactivity was used as an initial condition in the point kinetics equations. A comparison of the measured and calculated power and energy yield is shown in Figure 4.5 and Figure 4.10.

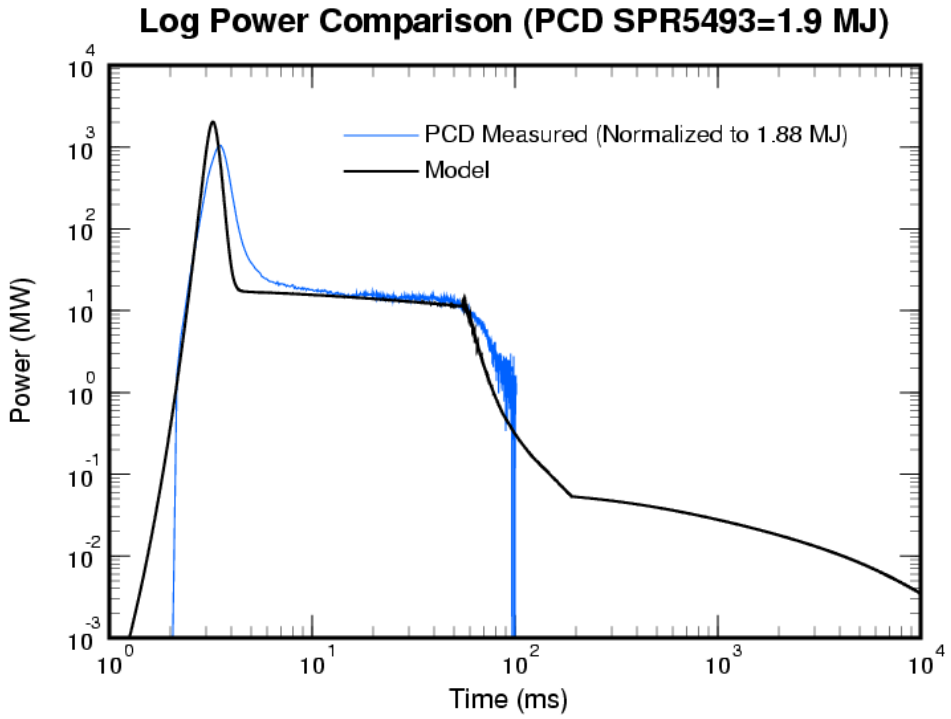

Figure 4.10. PCD Measured and Calculated Reactor for a Small SPR-III Pulse (1.88 MJ)

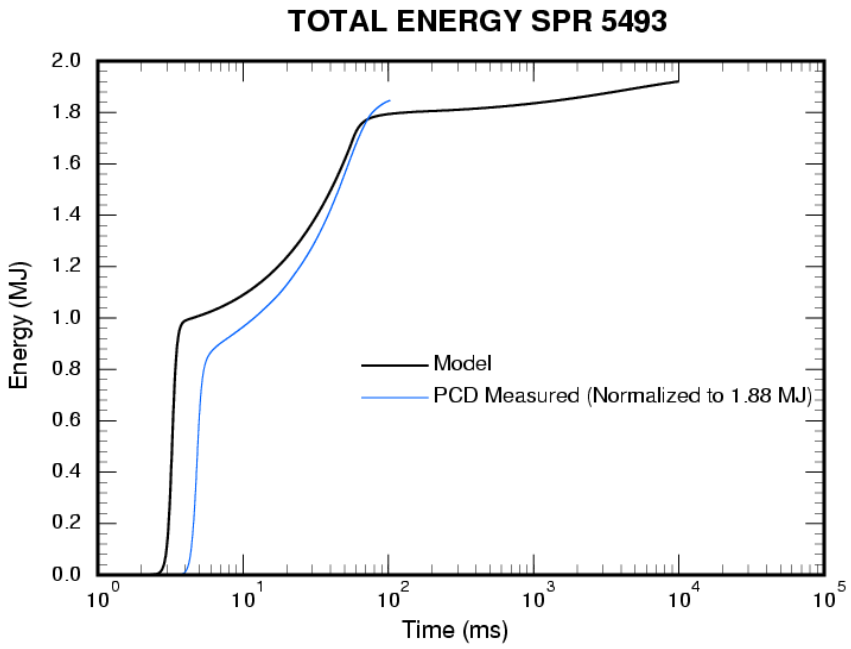

Figure 4.11. Measured and Calculated Energy Yield for a Small SPR-III Pulse (1.6 MJ)

The measured power history was normalized so that the area under the curve was equal to the energy derived from measured temperature rise.

In comparing the measured power and calculated power, it is obvious that there is a significant tail of reactor power after peak pulse. The first plateau in power is due to neutron multiplication of the delayed neutrons after peak pulse. The drop off at 55 ms is due to separation of the safety block. This causes the power to drop rapidly. However, after the safety block drop the model predicts that an additional 5% energy is deposited into the core over the next 10 seconds.

One discrepancy that is apparent when comparing the prediction and measured values is that the measured pulse width is greater than the model. The reason for the discrepancy between predicted and measured pulse width and shape is not understood. Several possibilities include

1. The reactor physics is not modeled correctly with point kinetics. However, this argument conflicts with the excellent agreement obtained with the 6 MJ pulse.
2. The massive concrete block adjacent to the reactor, which is not in the MCNP model, has a large effect for small pulses.
3. The MCNP model needs to be run with more geometric details of the reactor surroundings and with extended neutron lifetimes to obtain better lifetime estimates.
4. Neutron lifetime is complex time dependent parameter that is difficult to quantify.

The amount of energy contributed by the tail is significant. Approximately 40% additional energy is added during the tail of the pulse, and this amount is variable because safety block drop time may vary from test to test.

One interesting effect not shown in any of the power curves, but observed from fuel displacement predictions, is the absence of ringing in the fuel. For the large 6.6-MJ pulse, significant ringing is observed, similar to that seen in the test case. However, for the small 1.8-MJ pulse, there is no ringing observed in the model predictions. The reason is that the pulse full width, half maximum (FWHM) is approximately 1.5 ms, and this wide pulse width allows fuel expansion to keep up with the power as it is increasing.

4.5 Comparison to Published Measurements – Maximum 12 MJ SPR-III Pulse

Detailed power data for a maximum SPR-III pulse have been published in the Sandia Pulsed Reactor Facility (SPRF) Safety Analysis Report (SAR) (2005). The neutron lifetime and initial reactivity for a maximum pulse have been reported in the SPRF SAR (2005) as 15 ns and \$1.126. In the results that follow, 100% of the axial feedback coefficient was used because it should be the most accurate model for large pulses, using the reported values of neutron lifetime, initial reactivity, and 100% axial feedback results in the calculated power curve shown in Figure 4.12.

The power curve shown in the figure has a FWHM of 55 μs, which can be compared with the reported FWHM of 76 μs. The energy under the power curve is 12.6 MJ, which is very close to the reported 12-MJ maximum pulse value. The predicted reactor average and maximum temperatures are shown in Figure 4.1. A temperature rise of 450°C at the peak location is reported for a maximum pulse. This result is very close to the calculated value of 470°C; a difference of less than 5% in total energy yield.

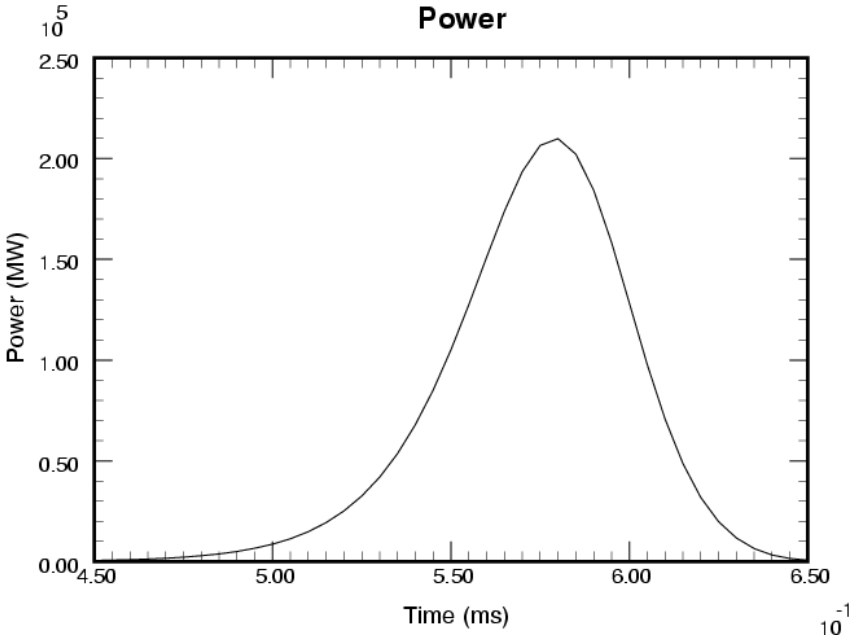

Figure 4.12. Calculated 12-MJ SPR-III Power Pulse, with 15-ns Neutron Lifetime and \$1.126 Reactivity Insertion (Maximum SPR-III Pulse)

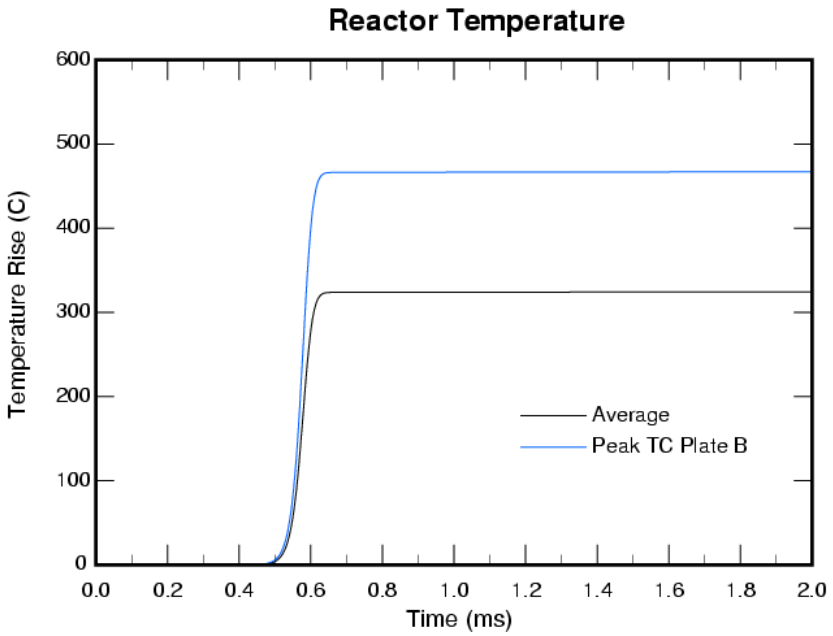

Figure 4.13. Calculated Core Temperature as a Function of Time for a Maximum SPR-III Pulse

The initial reactivity insertion was an instantaneous addition of $1.126. Figure 4.14 shows the calculated reactivity state of the reactor as a function of time predicted by the model. The reactivity becomes less than $1.00 (peak of the pulse power history in Figure 4.12) at ~0.58 ms. The pulse is virtually over at 0.65 ms. Note that at this point in time in Figure 4.14, the reactivity state is a positive ~$0.6. The maximum negative reactivity from fuel expansion occurs at ~0.75 ms, but the reactivity state is still a positive ~$0.44. Before the trough occurs in time, the axial expansion of the core forces the safety block electromagnetic coupling to be broken. Subsequently, the core becomes significantly subcritical. The safety block not only falls by gravity but is actually pushed away by the axial expansion. Protection circuitry also de-energizes the electromagnetic fields for the safety block and reflector elements, allowing them to fall by gravity to their least reactive position.

Also note that for Figure 4.14 and the subsequent figures, the oscillatory behavior of the fuel continues indefinitely. This indefinite oscillation does not occur in reality but instead dampens out over time. The oscillations would become smaller and smaller until an average value is reached. The model does not currently have an explicitly modeled damping mechanism, however numerical damping does occur when large time steps are taken.

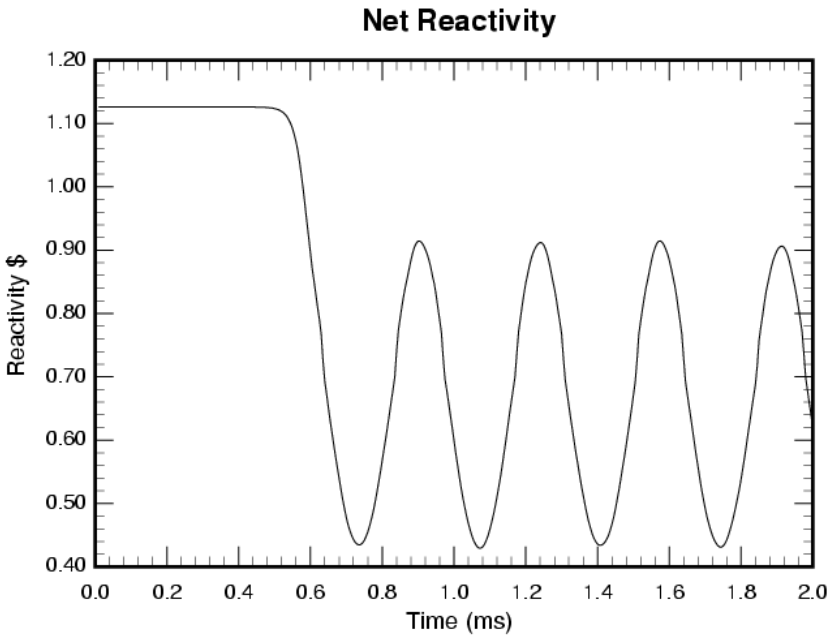

Figure 4.14. Calculated Reactivity as a Function of Time for a Maximum SPR-III Pulse

The radial and axial expansion and inner and outer radial displacements are shown in Figure 4.15 and Figure 4.16, respectively, as a function of time. Figure 4.15 shows that the radial expansion dominates the expansion behavior, with the axial expansion contributing only a small amount. In fact, if the axial expansion is ignored in the calculation, the reactor energy yield is 14.9 MJ vs. 12.6 MJ with axial expansion included, an increase of 18%. Thus, although the axial expansion is included in the calculation, it is not the dominant effect in the reactivity feedback.

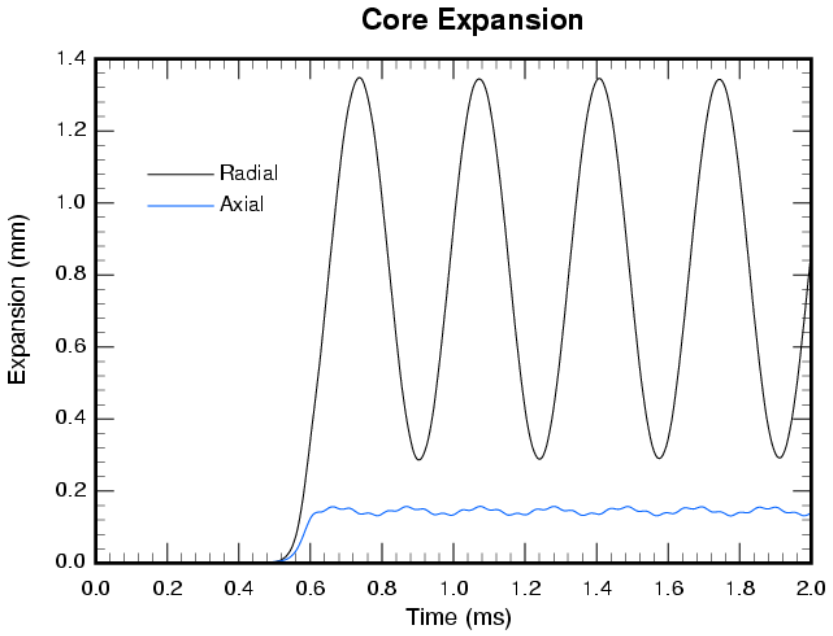

Figure 4.15. Calculated Outer Boundary Radial and Axial Expansions as a Function of Time for a Maximum SPR-III Pulse

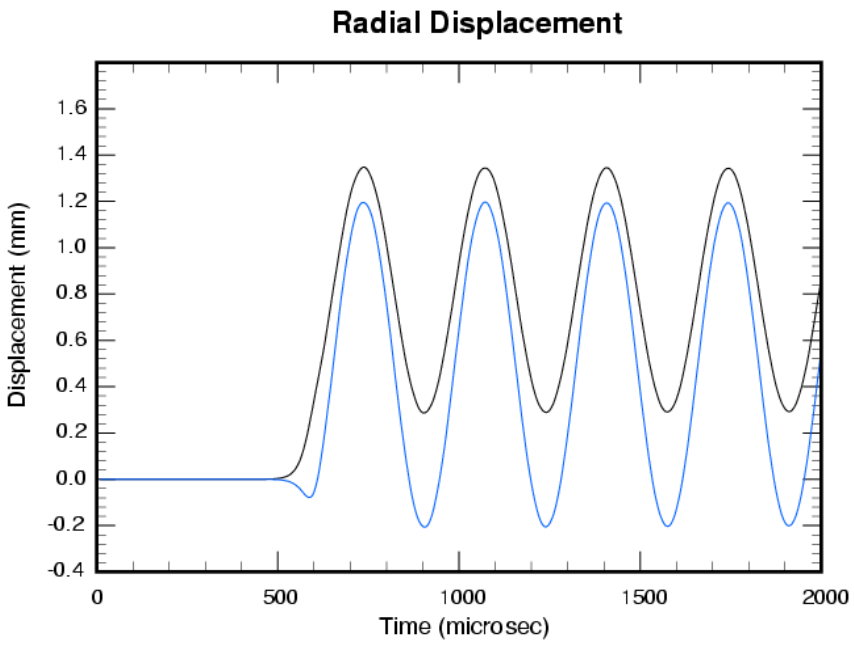

Figure 4.16. Calculated Inner (blue) and Outer (black) Radial Expansion and Contraction as a Function of Time for a Maximum SPR-III Pulse

The radial boundaries at the inside surface of the cavity and at the outside surface of the core can both expand and contract because they are unconstrained. The expansion of both inner (blue line) and outer (black line) radial boundaries is shown in Figure 4.16. It is interesting to observe that the inner cavity surface actually contracts during the cycle. The initial contraction displacement for the inner radius is less than 0.1 mm (0.01 cm). Using Table 3.4, this contraction would only add $0.002 (0.2 cents) of positive reactivity. At the same point in time, the outer radius has been expanded by ~0.2 mm (0.02 cm). Using Table 3.3, the outer surface radial expansion adds a negative $0.12 (-12 cents) of reactivity to the system. Hence, the feedback for the outer surface expansion dominates the reactivity effect.

Radial, tangential, and axial stresses and stains are calculated in the model as a function of time and location. The radial and axial fission density within the core causes a non-uniform temperature distribution to result. This temperature distribution is the driver for the shock wave and oscillatory behavior in the fuel plates. Figure 4.17 shows the volume averaged temperature distribution in radial direction for the core. This temperature distribution was calculated by using the fission density from MCNP results, the heat capacity of the fuel, and the total energy deposited in the core. Although thermal conduction is included in the model, the timing requirements are much greater than for the pulse duration. Hence, thermal conduction does not play a significant role in the analysis. The model assumes that this basic shape remains constant as a function of axial position in the core. The maximum and minimum radial temperature distributions within the core would have the same shape as shown in Figure 4.17 but have scale factors of 1.3 and 0.44, respectively.

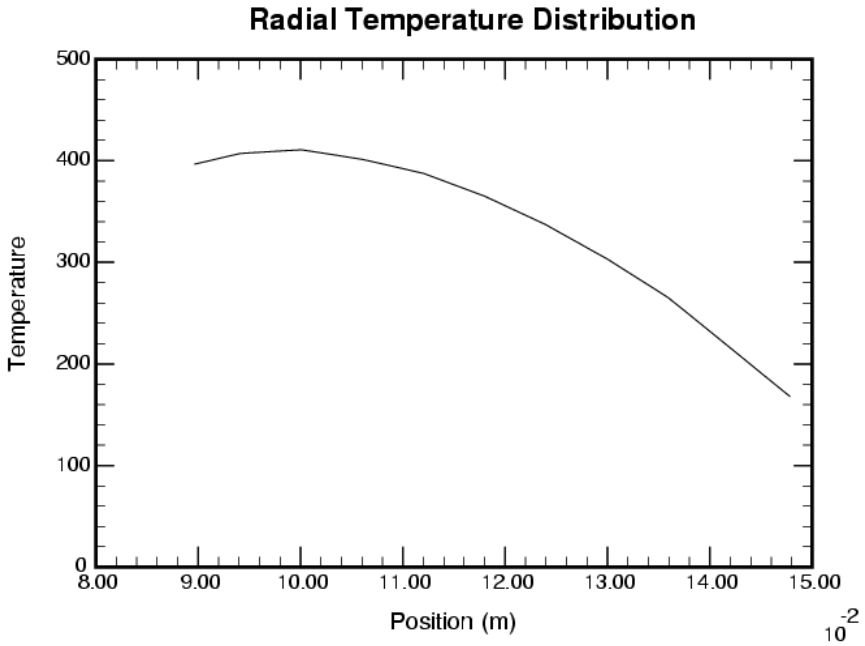

Figure 4.17. Volume Averaged Radial Temperature Distribution for a Maximum SPR-III Pulse

Figure 4.18 shows the model calculated average radial displacement (strain) for the core as a function of core radial position for a number of time periods in the first cycle. Prior to the power rise in the core, the displacement is zero. The first curved line above the zero value shows the inner portion of the core moving inward (contraction) while the outer portion of the core is moving outward (expansion). The core displacement then continues outward until the peak expansion is reached.

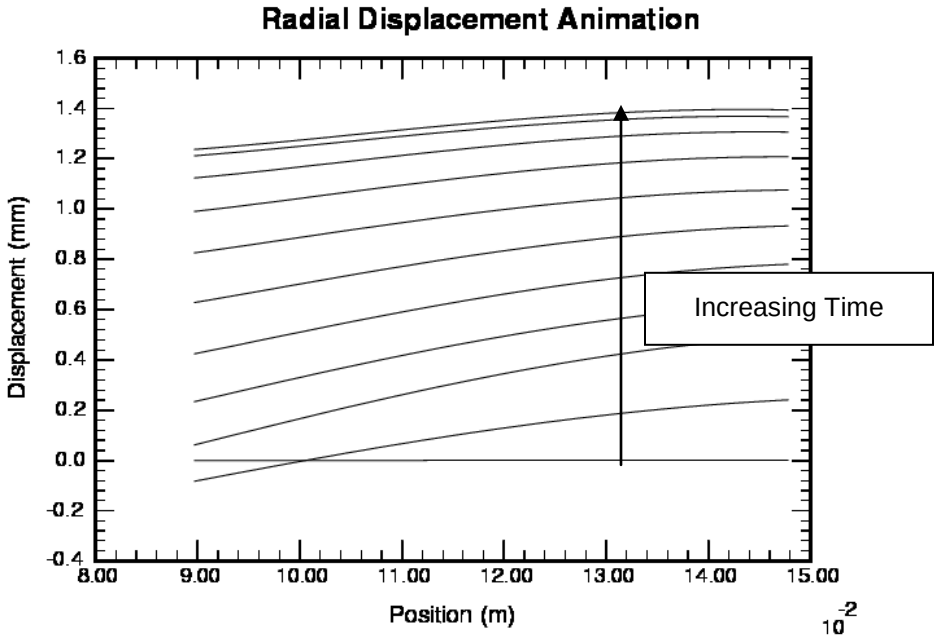

Figure 4.18. Calculated Radial Displacement (Strain) at Different Points in Time within a Cycle for a Maximum SPR-III Pulse

The stresses appear in two forms, radial and tangential (also known as hoop stress). These stresses are obtained by differentiating the radial displacement solution. The radial stress (outward directed) distribution at the axial core centerline is shown in Figure 4.19 at different time periods in the cycle (negative stress equals compression, positive stress equals tension). Initially, the stresses are zero and begin by going into compression. The maximum radial compression stress is calculated to be ~6.3 ksi. The stresses then rebound towards zero and become positive. The maximum radial tension is calculated to be ~3 ksi.

The yield strength (YS) and ultimate tensile strength (UTS) for cast U-10Mo as a function of temperature are shown in Figure 4.20. The YS and UTS are very similar up to 400°C, where they begin to diverge. Both values decrease as a function of temperature but plateau between 250°C and 500°C. At 400°C, the YS is approximately 65 ksi. The radial stresses shown in Figure 4.19 are at least a factor of 10 below this value.

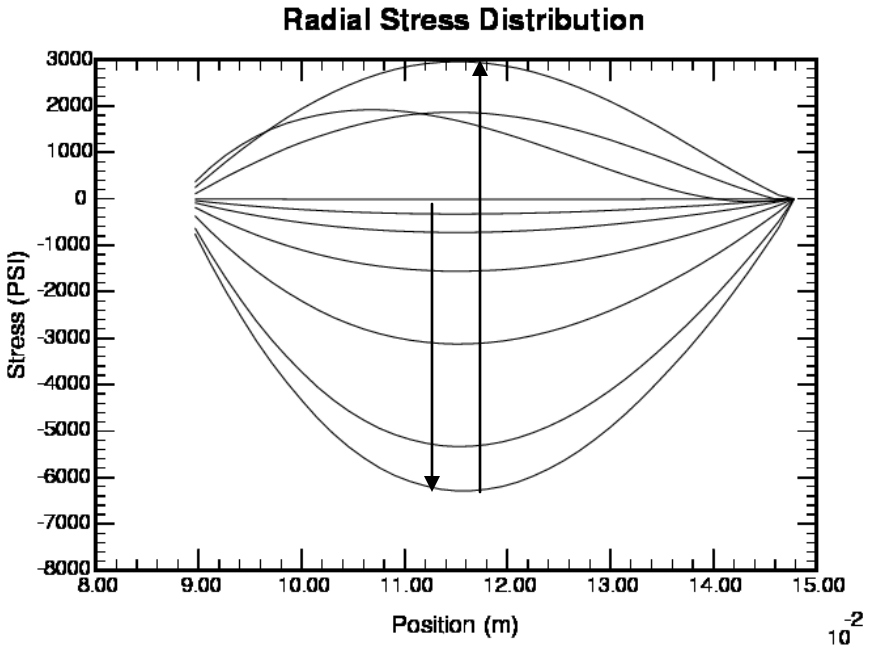

Figure 4.19. Calculated Radial (Outward Directed) Stress Distribution at Different Points in Time within a Cycle for a Maximum SPR-III Pulse

Arrows depict increasing time.

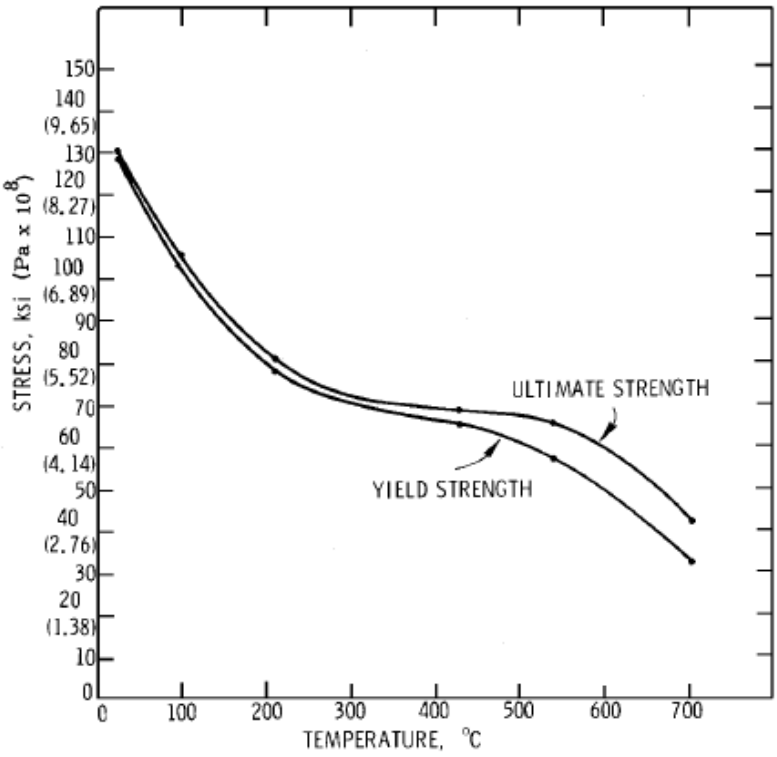

Figure 4.20. Yield Strength and Ultimate Tensile Strength for Cast U-10Mo as a Function of Temperature

The tangential stresses are found to be significantly larger than the radially directed stress. Figure 4.21 shows the results for the tangential stresses at the axial centerline of the core as a function of time for the outer core surface (blue line) and inner core surface (black line). The tangential stress distribution at the axial core centerline is shown in Figure 4.22 at different time periods in the cycle (negative stress equals compression, positive stress equals tension). The inner and outer surfaces represent the locations where the largest stresses are found. Initially, the stresses are zero. The inner surface begins by going into compression and then into tension. The outer surface begins by going very slightly into compression and then into tension. The maximum compressive stress is found on the inner surface of the fuel, ~100 ksi. The maximum tensile stress if found on the outer surface of the fuel, ~80 ksi. These values are above the 65 ksi YS value at 400°C. Normally this would be a problem. However, it has been shown that a rapid application of elastic displacement which causes the local stresses to exceed the YS for a short period of time does not result in failure of the material. Hoge (1965) estimated the required dynamic stress approximately twice the value observed in static or slowly (where slow is on the order of minutes) moving tensile tests before yielding of the material occurs. The maximum stresses are found to be within a factor of two of the yield strength.

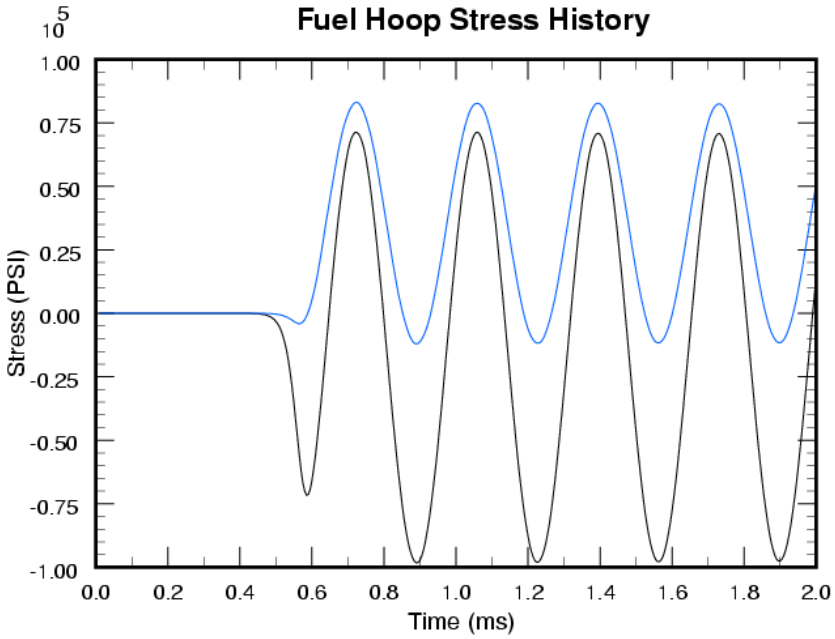

Figure 4.21. Calculated Tangential Hoop Stress as a Function of Time on the Outer (blue) and Inner (black) Boundary of the Average Fuel Plate for a Maximum SPR-III Pulse

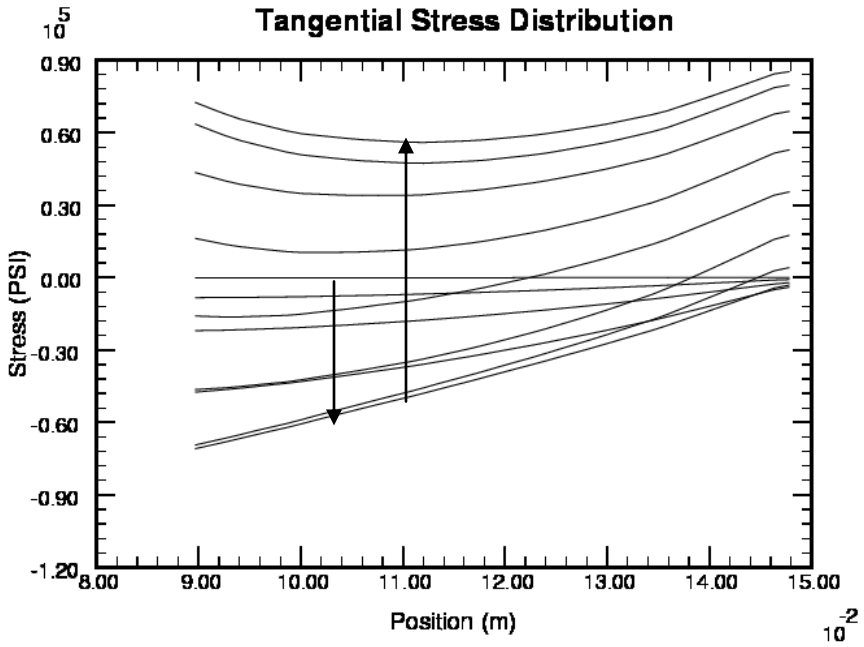

Figure 4.22. Calculated Radial Distribution of Tangential Stress at Different Points in Time within a Cycle for a Maximum SPR-III

Arrows depict increasing time.

The axial stresses are calculated independently from the radial stresses. The SPR-III reactor core is made of two identical core halves that are mirror images of each other at the axial centerline (SPRF SAR [2005]). Each core half contains nine fuel plates which are held together by a clamping ring and four symmetrically located Inconel bolts. During a pulse, the reflector elements are only partially inserted in the axial direction to account for the total reactivity desired for the pulse when the pulsing reflector is rapidly inserted to its full up position. Since the three reflector elements are only partially inserted into the core, the lower portion of the core will have a higher fission density than the upper portion due to the enhanced neutron reflection.

The axial temperature distribution at the outer radius of the core can be calculated by determining the fission density using MCNP. The result is shown in Figure 4.23. The total core axial length is ~13 cm with the mirror image at the centerline. The centerline is at 6.5 cm in Figure 4.23. The asymmetry and jagged shape are due to the neutron reflection asymmetry, described above, and the geometrical and mass differences of the fuel near the axial centerline of the core.

To determine the axial displacement and axial stresses in the fuel, the model uses only the lower core half. The lower-half core temperature, used in the model, is shown in Figure 4.24. The half core length is from 5 cm to 11.5 cm. Including the clamping ring and Inconel bolt, the total length (core, ring, and bolt) is from 0 cm to 16 cm.

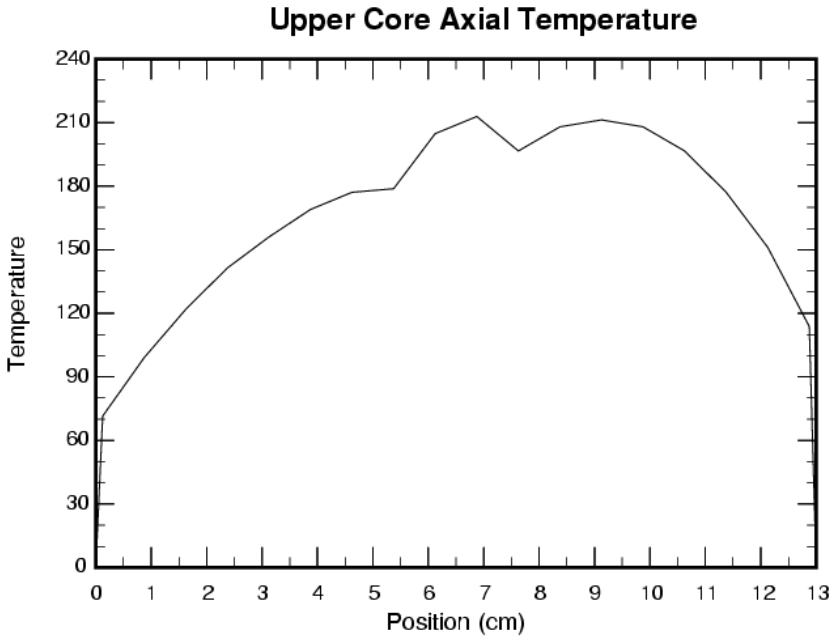

Figure 4.23. Axial Temperature Profile at the Outer Radial Boundary of the Core Following a Maximum SPR-III Pulse

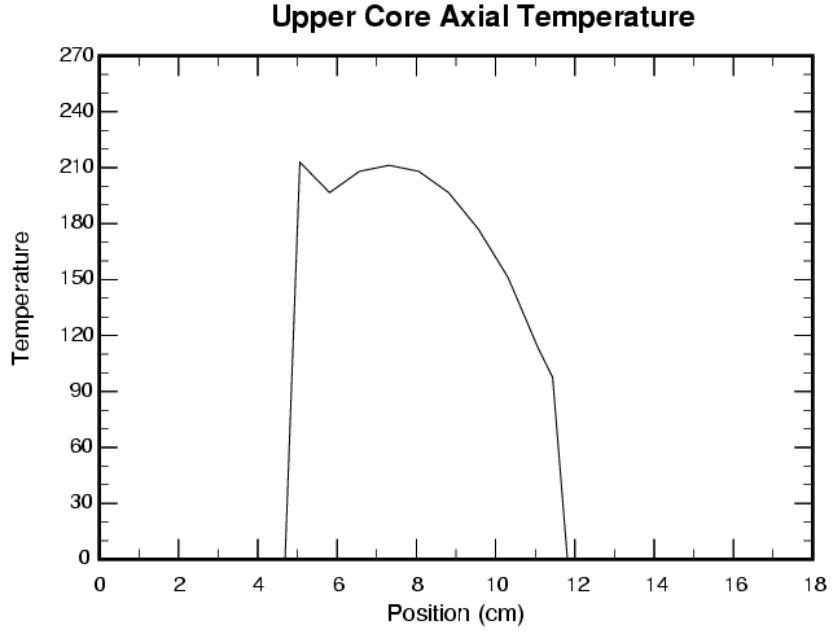

Figure 4.24. Lower Half Core Axial Temperature Profile Following a Maximum SPR-III Pulse

The heating of the core causes an axial displacement. Figure 4.25 shows the axial displacement of the outer fuel ring, steel clamps, and Inconel bolts at the initial displacement and at the maximum displacement. The calculation was made with the bolt mid-plane being the zero coordinate. This coordinate system was chosen so that the initial displacement (due to bolt stress) could be used as a fixed boundary condition for the duration of the pulse.

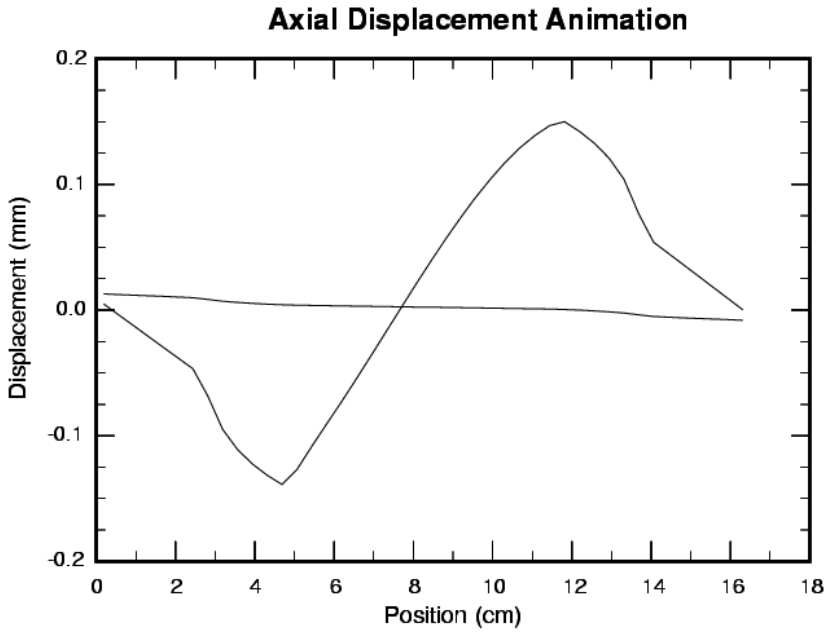

Figure 4.25. Calculated initial and Final Axial Displacements of the Outer Fuel Ring, Steel Clamps, and Inconel Bolts Both During and After a Maximum SPR-III Pulse

The axial displacement gives rise to a reactivity feedback effect, which was derived by the change in displacement for the fuel at the 11.5-cm position. Figure 4.26 shows the overall axial fuel expansion as a function of time.

The axial stress in the fuel plates is confined to the outer 1-cm edge of each fuel plate. As discussed earlier, gaps are placed between the fuel plates to reduce stress and reduce the feedback effect of axial displacement.

The axial stress distribution for the lower core half is shown in Figure 4.27. The axial stress includes the stress in the outer 1 cm of fuel, the steel clamping rings, and the Inconel bolts. The Inconel bolts run from 0 to 3 cm and 14 though 17 cm. Miller (1994) calculated the bolt stress induced during a maximum pulse using the combination of three-dimensional finite-element stress codes JAC3D and PRONTO3D. JAC3D was used to establish the initial bolt and fuel stress conditions of the pre-pulsed SPR-III reactor. Subsequently, PRONTO3D was used to predict the transient stress distribution for a prescribed power pulse. The pre-pulsed stress condition of the bolts could not be simulated with the current one-dimensional model because there exist three-dimensional leveraging effects of the steel clamping rings that can only be captured by a multidimensional code, such as JAC3D. In the current one-dimensional model, the modulus of elasticity of the steel clamping rings is reduced to account for the three-dimensional leveraging effects. Thus our one-dimensional model can be adjusted to generate nearly the same result as the combined JAC3D-PRONTO3D code. To simulate the three-dimensional leverage effect in one dimension, the steel clamping ring modulus of elasticity is reduced to make the rings softer so they can absorb some of the fuel displacement without overstressing the bolts. If the steel clamping ring modulus is not reduced, an over-prediction of the bolt stress will result. For the case with the modulus not reduced, the bolt stress is approximately 150 ksi vs. ~80 ksi with the modulus

reduced. This modification of the one-dimensional model to account for three-dimensional effects allows the axial expansion to be calculated more accurately.

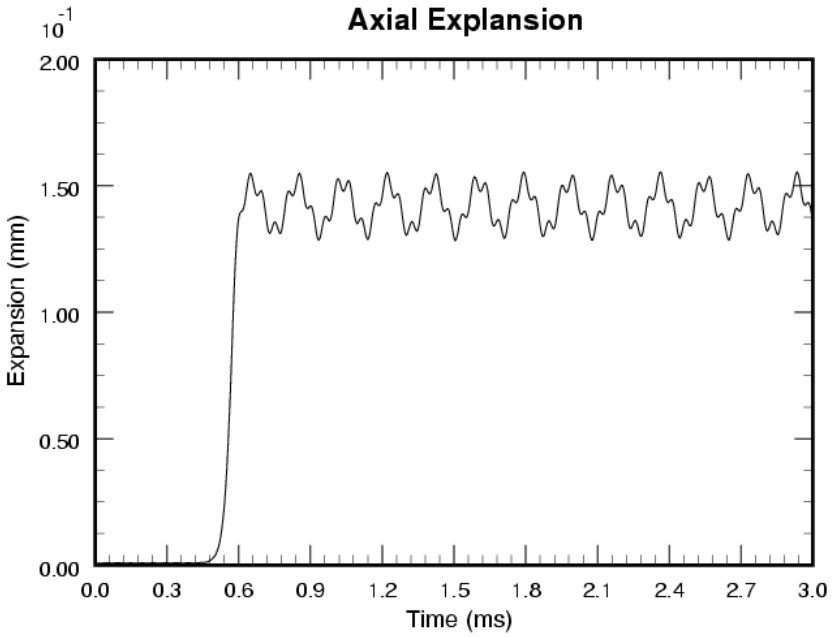

Figure 4.26. Calculated Axial Expansion as a Function of Time for a Maximum SPR-III Pulse

Figure 4.28 shows the calculated axial stress in the fuel and the bolts as a function of time. Note that the bolt mid-plane stress oscillates about an average value of ~80 ksi. The figure also illustrates the magnitude of the stress ringing in the fuel and bolts.

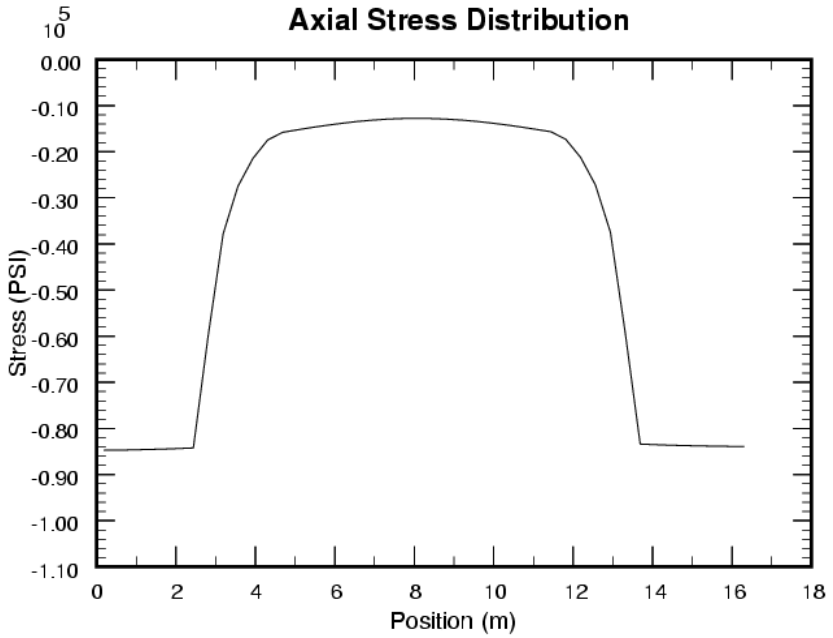

Figure 4.27. Calculated Axial Stress Distribution Including Fuel, Steel Clamp Rings, and Inconel Bolts Following a Maximum SPR-III Pulse

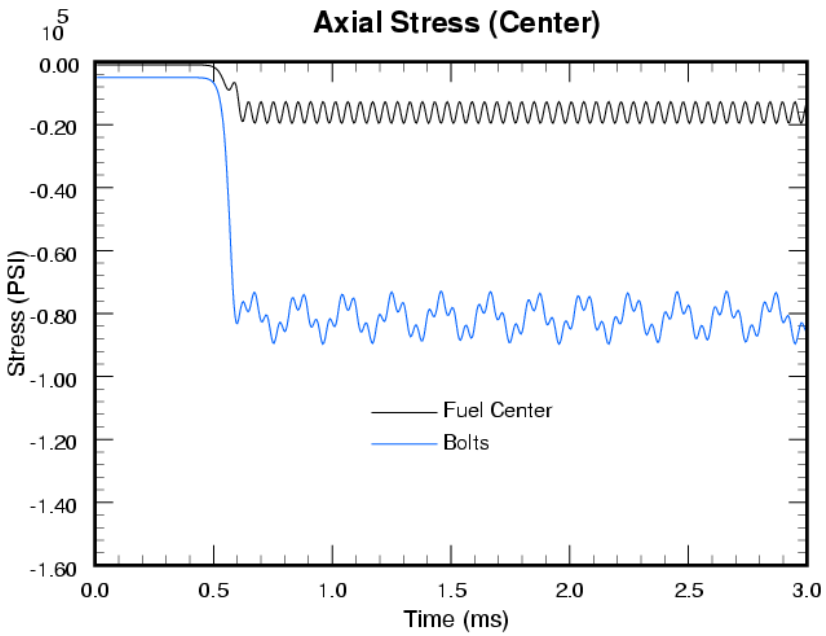

Figure 4.28. Calculated Axial Stress as a Function of Time for the Fuel Center Plate and the Bolt Mid-Plane for a Maximum SPR-III Pulse

4.6 Summary and Conclusions

A coupled point-reactor kinetics, elasticity, and thermal reactor model has been developed to demonstrate how well a simple model can predict the pulse performance in SPR-III, with the intention of application to EDNA type devices. The neutronics code MCNP is used to predict reactor feedback as a function of core temperature and expansion and to determine the fission-density distribution in the core. Finite difference techniques are used to solve the radial and axial transient elastic expansion equations and a simple thermal energy equation of the reactor fuel. Effects that are typically considered negligible are included in the model, such as delayed neutrons and thermal conduction. This allows the model to be used for longer transients. The transient elastic-displacement equations, that relate thermal expansion, mass inertia, and mechanical stress/strain, were taken from previous work by Reuscher (1969).

A demonstration calculation of the SPR-III reactor results in good agreement with actual SPR-III behavior. Detailed comparison to a maximum pulse (12 MJ) and large pulse (6 MJ) were quite good for overall pulse shape and energy production.

The comparison to a small pulse (1.88 MJ) was good, over-predicting the pulse energy by approximately 10% and total energy by 3%. The model predicts a pulse width significantly shorter than measured, by almost a factor of two. The reason for the discrepancy for very small pulses is unknown and requires further study. However, for applications related to EDNA type devices, the model should performed adequately, since the major concern is for large pulses involving tens of mega joules of energy deposition in the core.

5 Applications to ZEDNA

The previous sections of this report demonstrate that the dynamic reactor model is ready for application to, or use in development of, a specific ZEDNA design using plate type fuel. Several safety-based calculations will be performed. However, before performing any safety or off-normal calculations, a best estimate calculation will be made to show how the reactor is expected to perform.

There exist some neutronic differences between the ZEDNA reactor and SPR-III. The estimated neutron lifetime is 73 ns. The delayed neutron fraction is 0.0073, and a Doppler coefficient is tabulated below as a function of temperature.

Table 5.1. ZEDNA Doppler Feedback Coefficient as a Function of Temperature

Fuel Temperature (K)	Reactivity ($)
293	0.0
400	-.064322
500	-.078378
600	-.078378
1200	-.082432

As before, a series of MCNP reactivity calculations were performed for fuel axial, inner, and outer radial expansion. In addition, a series of calculations for reactivity as a function of safety block drop were also performed. The results of these reactivity calculations are shown in the tables below.

Table 5.2. ZEDNA Reactivity as a Function of Outer Radial Expansion

Outer Radius Expansion (mm)	Reactivity ($)
0.0	0
.1	-0.00405
.2	-0.02297
.3	-0.03514
.4	-0.04865
.6	-0.07162
.8	-0.10946

Table 5.3. ZEDNA Reactivity as a Function of Inner Radial Motion

Inner Radius Expansion (mm)	Reactivity ($)
0.0	0
-.1	0.0017
-.2	0.0189

Table 5.4. ZEDNA Reactivity as a Function of Axial Expansion

Axial Expansion (mm)	Reactivity ($)
0.0	0
.1	-0.00146
.2	-0.02297
.3	-0.04054
.4	-0.04865
.5	-0.06757
.6	-0.07622
.7	-0.09459
.8	-0.12162

Table 5.5. ZEDNA Reactivity as a Function of Inner-Core Safety Block Drop

Core Position (cm)	Reactivity ($)
0.0	0
.5	-0.15676
1	-0.21351
1.5	-0.28514
2	-0.42027
2.5	-0.50541
3	-0.65135
4	-0.91216
10	-2.53243
20	-5.26622
30	-7.62027
46	-10.9135

The change in fuel radius in the gap region was assumed negligible.

5.1 Normal ZEDNA Operation

The performance of the ZEDNA reactor under normal operational parameters was calculated. This calculation is provided so that the reader has a basis of comparison for all off-normal cases.

An EDNA device operates quite differently from an FBR. An FBR inserts a reactivity above $1.00 which creates a super prompt critical state with an initial neutron population of zero. A stray neutron triggers the chain reaction that leads to the pulse, and core expansion shuts down the reactor. An EDNA device does not operate in the super prompt

critical regime. Instead, it is operated in a subcritical, delayed critical, or supercritical state. A pulse of external neutrons is injected into and multiplied by EDNA into a significant pulse. Subsequently, the neutron population decays exponentially with time. If the reactivity is still above zero after the pulse, an EDNA core must be shut down by some means such as a safety block drop,

The expectation is that the ZEDNA reactor is to be operated by bringing the reactor to an initial reactivity level of $.80 positive, which results in a period on the order of 1 second. During the time at which power is slowly rising with a 1-second period, the Z machine is activated (in this example at 0.1 ms) which sends a pulse of neutrons into ZEDNA. The neutrons are multiplied and decay away with time. Shortly after the pulse, the safety block is separated (at 55 ms) shutting down the reactor.

This sequence of events is depicted in the power and temperature curves shown in Figure 5.1 and Figure 5.2.

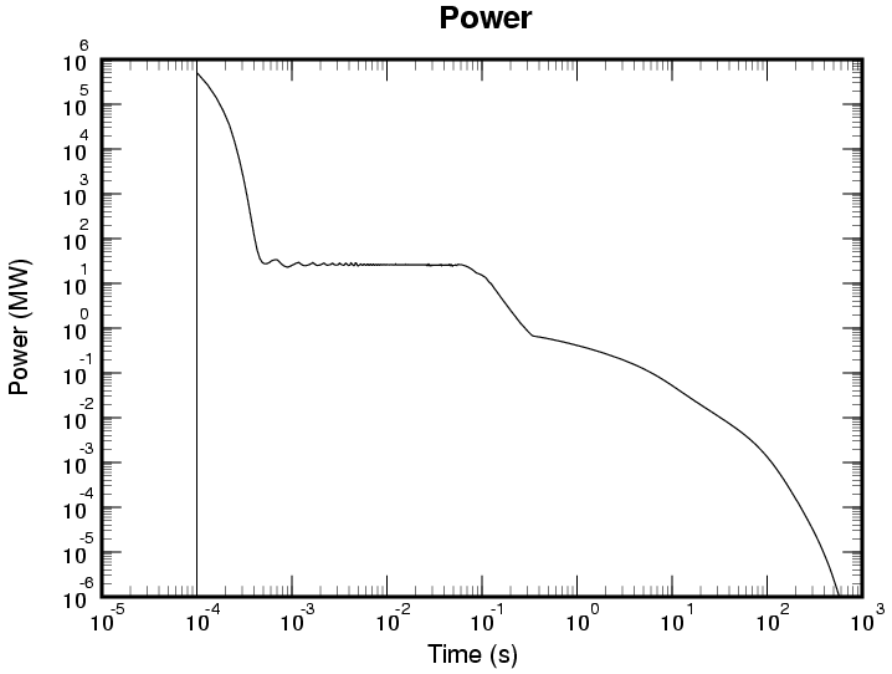

Figure 5.1. Expected Power History from a Normal ZEDNA Operation

The Z Pulse is at 0.1 ms, and the safety block drop is at 55 ms.

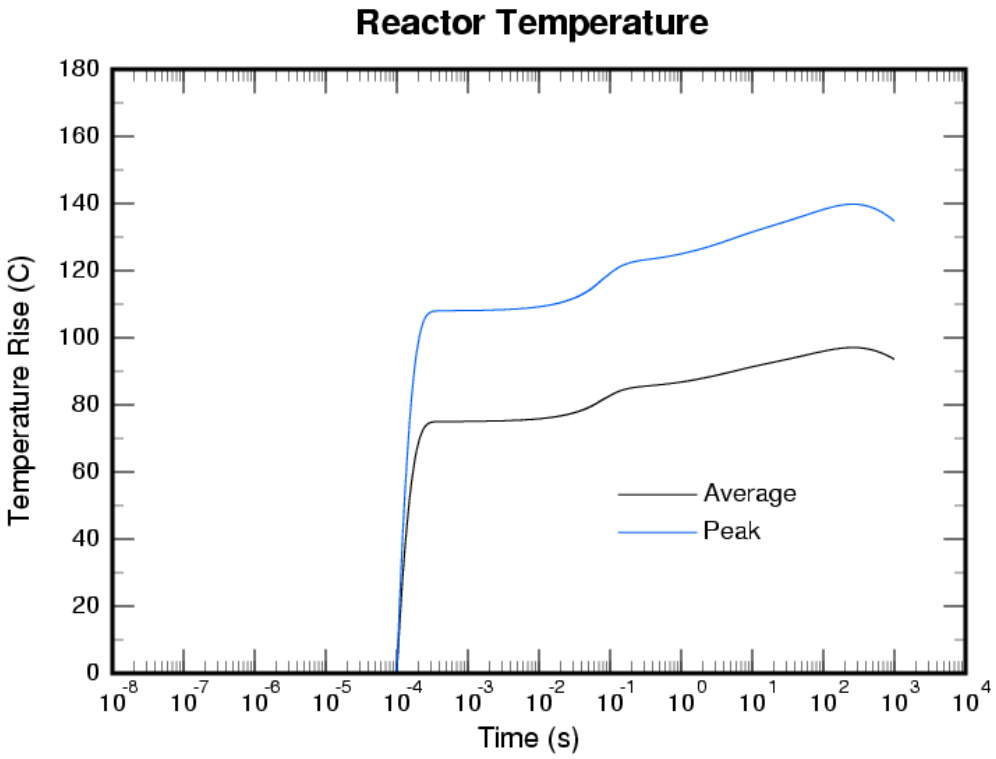

Figure 5.2. Expected Temperature History of the Reactor during a Normal ZEDNA Operation

The thermal boundary conditions for the ZEDNA reactor are currently set to a fixed heat transfer coefficient of 30 W/m^2K. This causes the temperature to turn around at approximately 250 seconds. During this time, power is generated in the reactor due to the effect of delayed neutrons. Note that the temperature rise (which is proportional to energy deposition) during the tail of the pulse is on the order of 25%. Such large energy depositions are significant if one is using dosimetry to evaluate pulse size.

Figure 5.3 illustrates the effect of Doppler and expansion feedback on the total energy yield in ZEDNA.

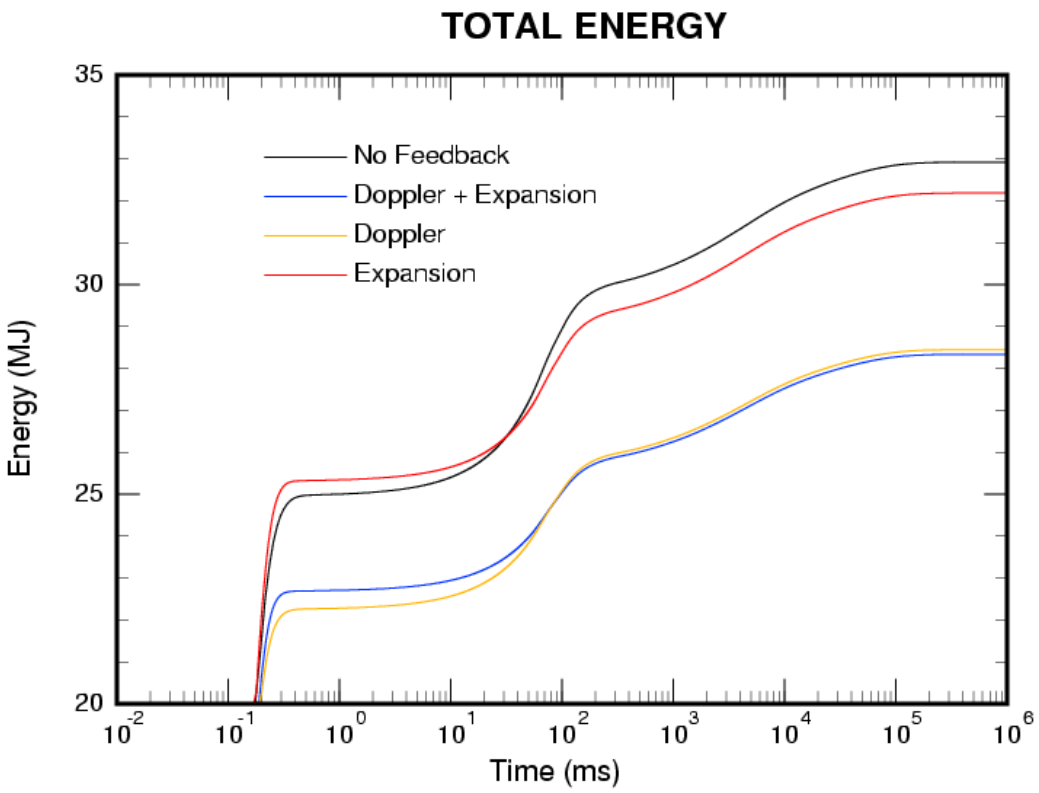

Figure 5.3. The Energy Yield as a Function of Reactivity Feedback

Note - the Y-axis begins at 20 MJ for enhanced detail.

The first, black curve in Figure 5.3 shows what the energy yield will be in the case of no feedback. Without feedback, the neutron pulse is multiplied yielding approximately 25 MJ of energy. If only Doppler feedback is included, the energy yield is reduced to approximately 22 MJ. If only expansion feedback is included, there is actually an increase in initial energy yield because the inner radius expands before the outer radius. And finally, when all feedback effects are included the net pulse yield is 22.5 MJ, i.e., a loss of 2.5 MJ (10%) compared to the case of no feedback.

5.2 ZEDNA Reactor Control

When bringing the ZEDNA reactor to its pre-pulse condition of a 1-second period, the rector operator will be adding reactivity. One question that can be answered with this model is how much energy is deposited in the reactor before the 1-second period is attained, as a function of reactivity insertion rate. The model was run with two slow reactivity insertion rates of $.01 and $.05 per second. The resulting energy yields when a 1-second period (equivalent to $.80 reactivity) was attained are 4 MJ for the $.01 per second insertion rate and 2.2e-6 MJ for the $.05 per second insertion rate. From these modest values of energy yield, it can be concluded that the ZEDNA reactor will not overheat during the pre-pulse reactivity insertion operation, even with very slow insertion rates, i.e., $.01 per second.

5.3 Off-Normal ZEDNA Cases

Several off-normal type ZEDNA operations were investigated which could hypothetically occur if hardware failures or other types of mistakes are made.

The first off-normal operation consists of too much initial reactivity, which causes a ZEDNA pulse similar to a SPR pulse. The off-normal calculation consists of reactivity insertion over \$1.00 but limited to \$1.05. The \$1.05 limit is assumed based upon current preliminary ZEDNA reflector designs. Such an operation leads to a self-initiated reactor pulse and is further assumed to be followed by a Z-pinch. The first pulse occurs naturally because the reactivity is over \$1.00. The second pulse is assumed to occur because hardware was unable to stop the Z machine from initiating a pulse. This double pulse causes the maximum energy yield conceivable in this type of off-normal operation.

In the first case, the reactivity is assumed to be added at \$.25 per second up to a maximum of \$1.05. The initial reactivity was set to \$.95 to shorten the run time. The ZEDNA reactor was found to initiate a pulse at approximately 230 ms. The first pulse was followed by a Z-pinch 50 ms later; the safety block was dropped another 50 ms later. The resulting power curve is shown in the Figure 5.4 below.

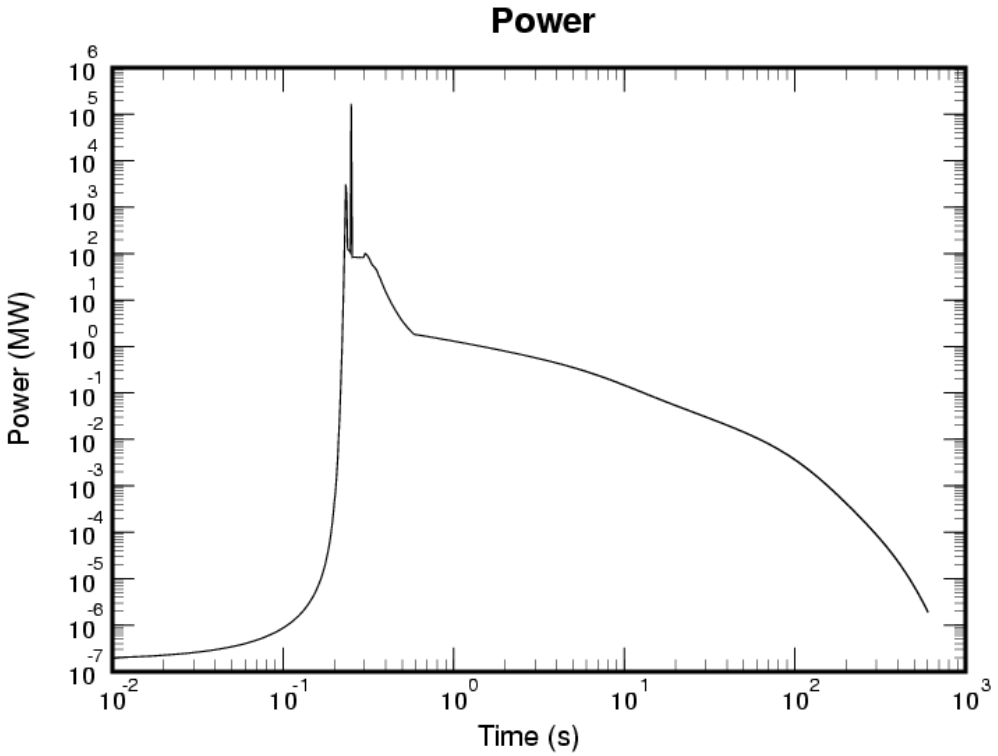

Figure 5.4. The ZEDNA Power History in an Off-Normal Double Pulse where the First Pulse is Due to Over-Reactivity and the Second is Due to a Z-Pinch

The time scale in Figure 5.4 goes out approximately 15 minutes to give the reader an idea of the full power history. The pulse detail is shown in Figure 5.5, which is plotted on a linear time scale.

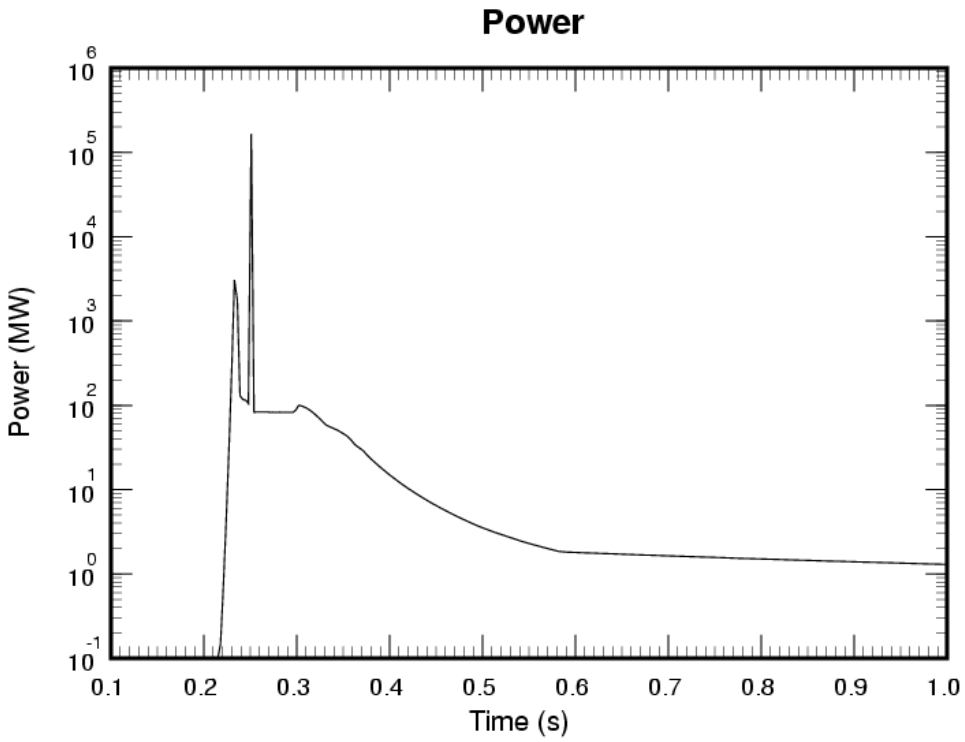

Figure 5.5. Detail of the Power History in an Off-Normal Double Pulse Operation

The first pulse shown in Figure 5.5 is the self-induced ZEDNA reactor pulse. The second pulse is due to the Z-pinch. The plateau that follows is due to multiplication of delayed neutrons. The drop in power after the plateau is due to safety block drop. The final plateau occurs after the safety block comes to rest (at 0.6 seconds).

The slight rise in power before the safety block drop is a numerical artifact caused by releasing the fixed axial boundary condition at the core mid-plane. When the fixed displacement boundary condition is released, the core relaxes but in the direction of adding reactivity, i.e., the two core halves move toward each other at a rate faster than the falling velocity. Of course, this cannot happen because the two core halves actually push on one another. The slight error introduced by this numerical artifact is negligible in terms of the overall model behavior, but it may appear in some cases when a safety block drop occurs.

The reactor temperature due to the double pulse is shown in Figure 5.7.

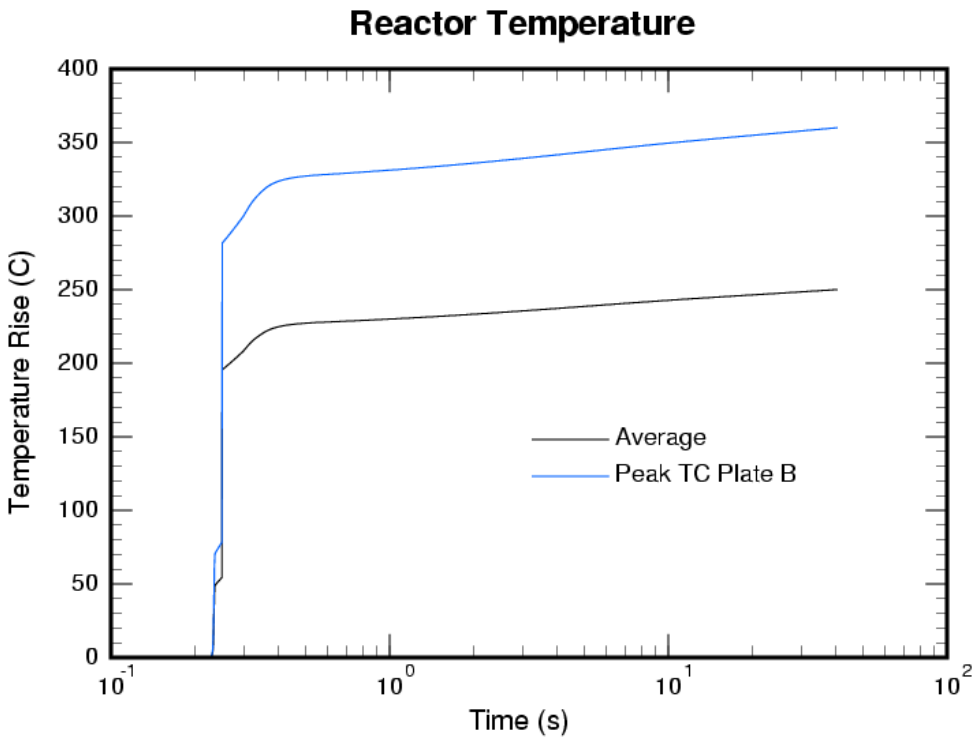

Figure 5.6. ZEDNA Reactor Temperature from an Off-Normal Double Pulse Operation

As shown in Figure 5.6, the maximum temperature rise of the ZEDNA reactor is expected to be less than 400ºC. This temperature rise is similar to SPR-III during a normal operation. It appears that this type of off-normal double pulse event will not jeopardize the integrity of the ZEDNA reactor. However, because the fuel plate size is larger than in SPR, fuel cracking could occur if the fuel is not segmented appropriately.

The reactivity associated with an off-normal double pulse operation is shown in Figure 5.7. The initial slight positive slope is due to the $.25/sec reactivity ramp. The drop at 23 ms is due to the first pulse, which brings the reactivity below $1.00. The next drop is due to the Z-pinch, which causes a further drop in reactivity—to approximately $.70 positive. The final drop in reactivity at 0.3 ms is due to safety block drop.

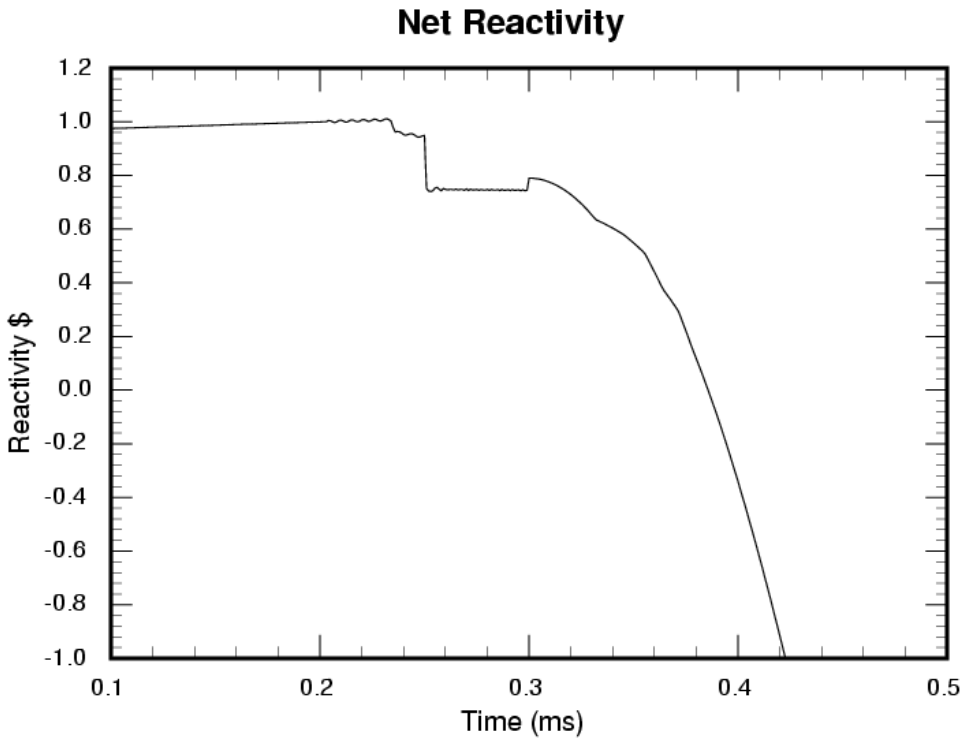

Figure 5.7. Reactivity of an Off-Normal Double Pulse Operation

Note that although there was a $1.05 reactivity limit, that limit was not reached before the first pulse. Hence, additional cases with higher reactivity limits would have identical behavior. However, higher reactivity insertion rates would allow the pre-set limit to be reached before the pulse.

The next off-normal ZEDNA operation to be examined is a very large Z-pinch source, larger by a factor of 4. In performing this calculation, the neutron source term in the point kinetics equations was increased by a factor of 4. The resulting power, energy, and temperature history are shown in Figure 5.8 through Figure 5.10.

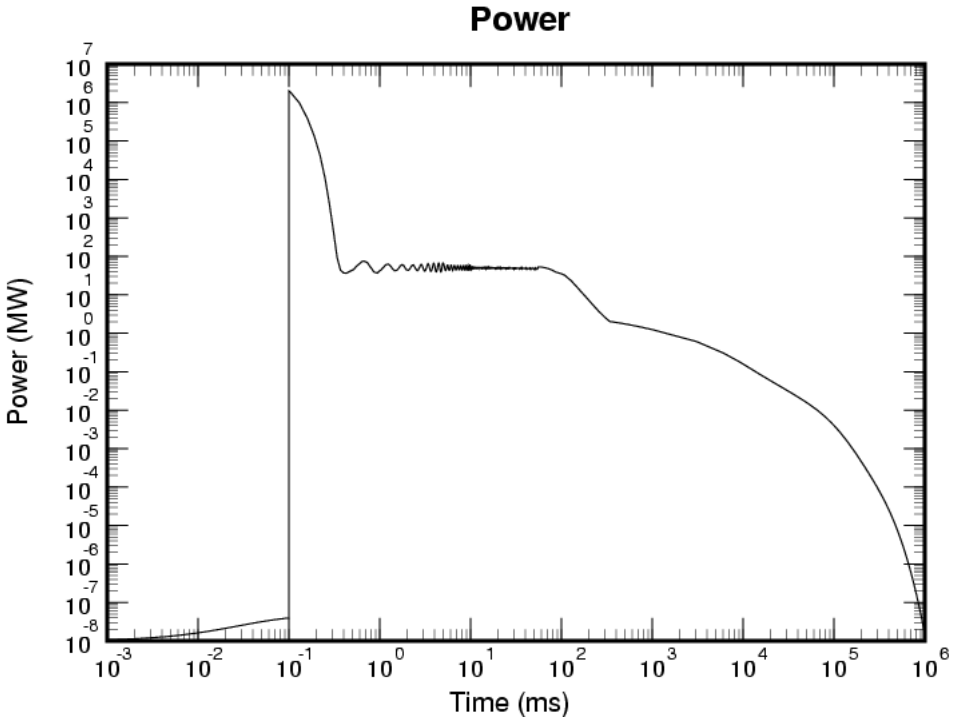

Figure 5.8. Power History of ZEDNA when the Z-Pinch Source Term is Increased by a Factor of 4

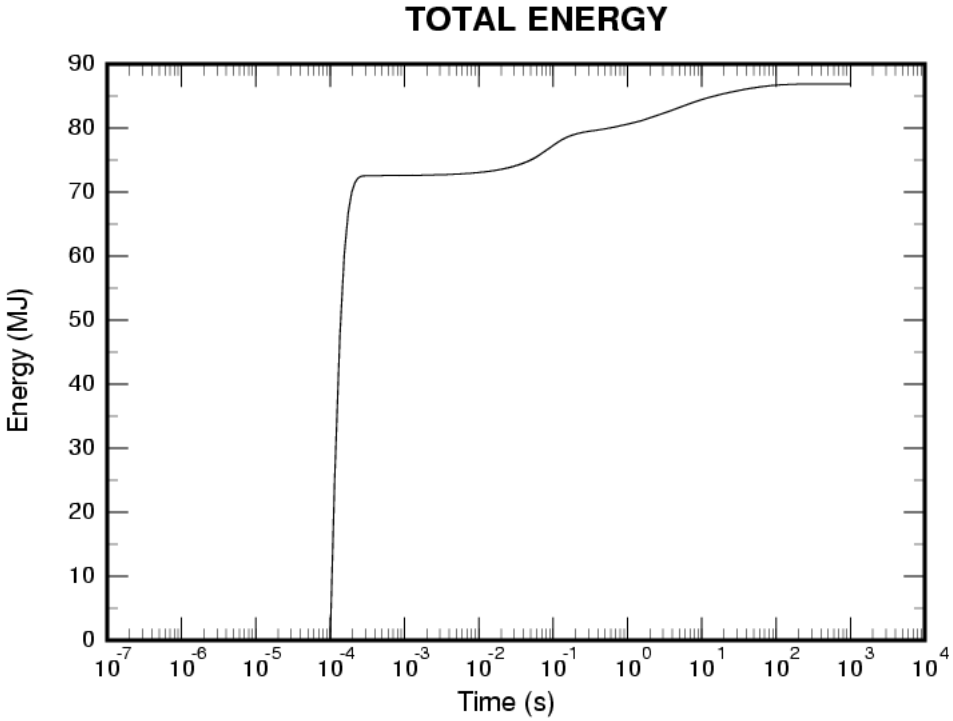

Figure 5.9 Energy History of ZEDNA when the Z-Pinch Source Term is Increased by a Factor of 4

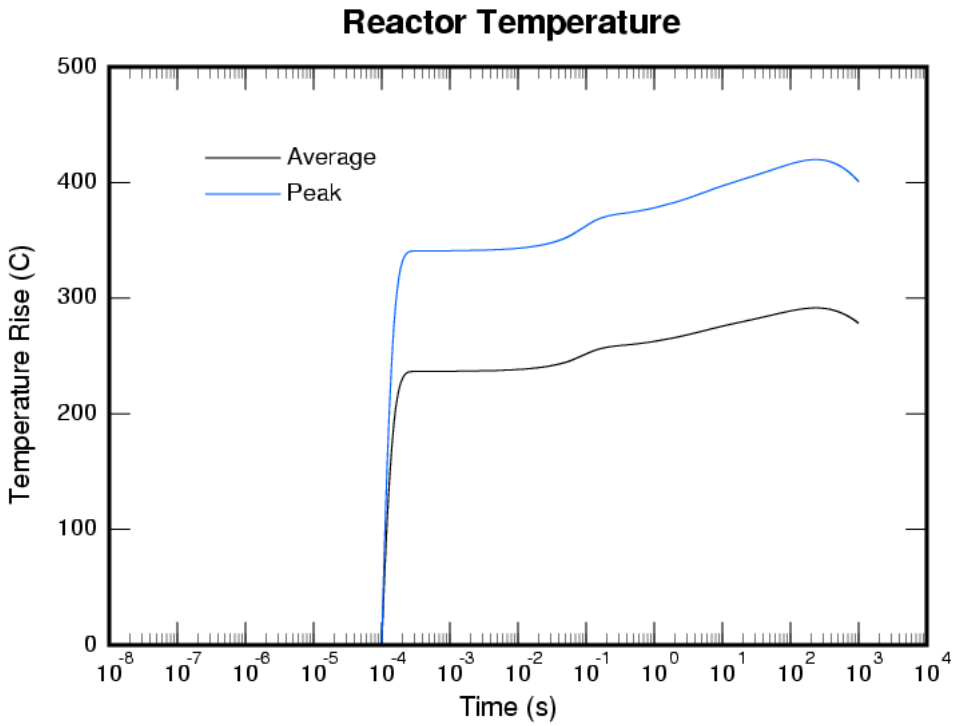

Figure 5.10. Temperature History of ZEDNA when the Z-Pinch Source Term is Increased by a Factor of 4

The predicted peak temperature history is expected to be approximately 400ºC rise. Again, this is similar to a typical SPR pulse and is not expected to jeopardize the ZEDNA reactor.

5.4 Worst Case ZEDNA Accident Scenario

Several off-normal type ZEDNA operations were investigated which could hypothetically occur if hardware failures or other types of mistakes are made. However, for the purpose of safety analysis a worst possible case is hypothesized. In this worst possible case, the reflector control rod is assumed to add reactivity at the rate of $.25 per second, as designed, but an over-reactivity condition occurs which causes the reactivity to exceed $1.00, and the reflector reactivity is continued to a maximum of $1.05 total reflector reactivity. This case has been previously analyzed in ZEDNA off-normal cases. However, to consider a worst case scenario, it is hypothesized that the core safety block does not split after the pulse, and the reactor remains in a supercritical condition until core expansion and Doppler reduce the reactivity to subcritical conditions. The resulting power, energy and reactor temperature from the worst-case scenario are shown in Figure 5.11, Figure 5.12, and Figure 5.13.

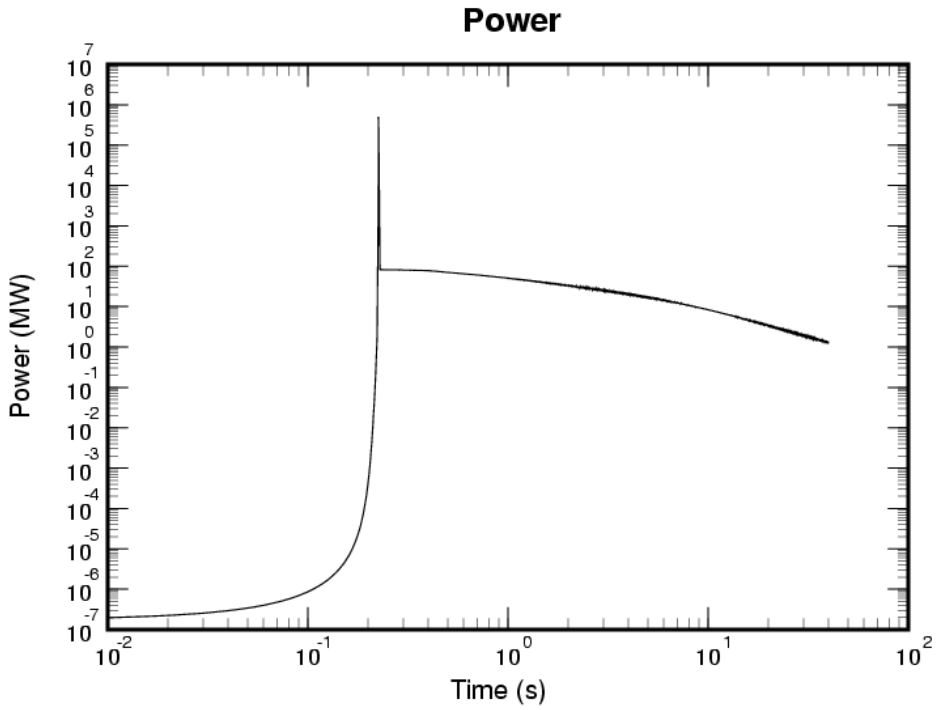

Figure 5.11. Power History of ZEDNA in a Worst Possible Accident Scenario

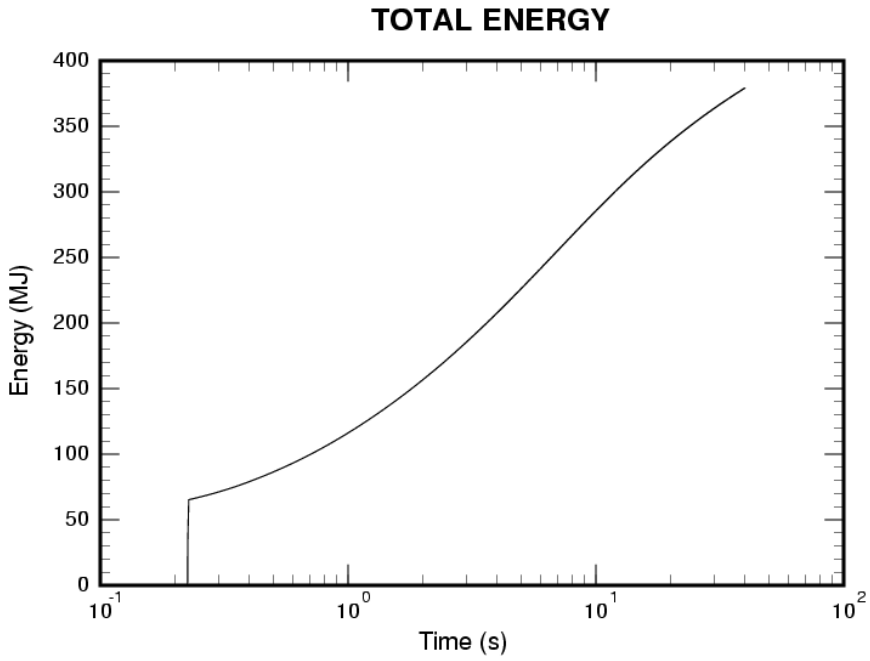

Figure 5.12. Energy History of ZEDNA in a Worst Possible Accident Scenario

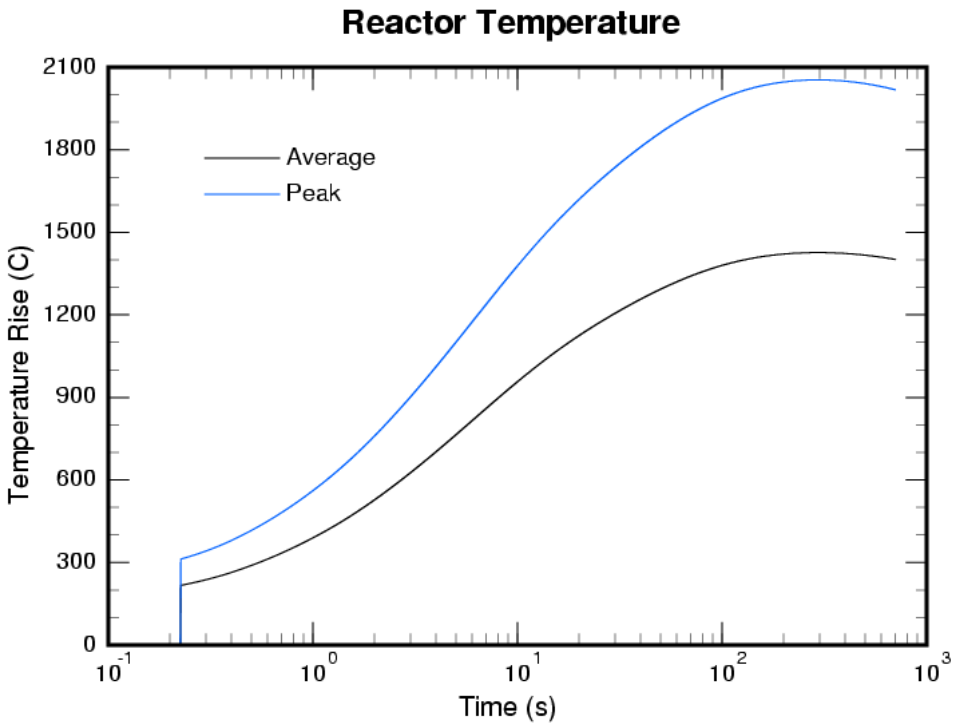

Figure 5.13. Temperature History of ZEDNA in a Worst Possible Accident Scenario

The predicted temperature history indicates that the reactor would get very hot, most likely melting the fuel (melt temperature of U10Mo is 1130ºC). However, this prediction is based upon large extrapolations of material properties, which have only been measured up to 600ºC.

In addition, the temperature history is in the range where the reactivity feedback effects are linearly extrapolated from the MCNP reactivity tables. The predicted reactivity is shown in Figure 5.14.

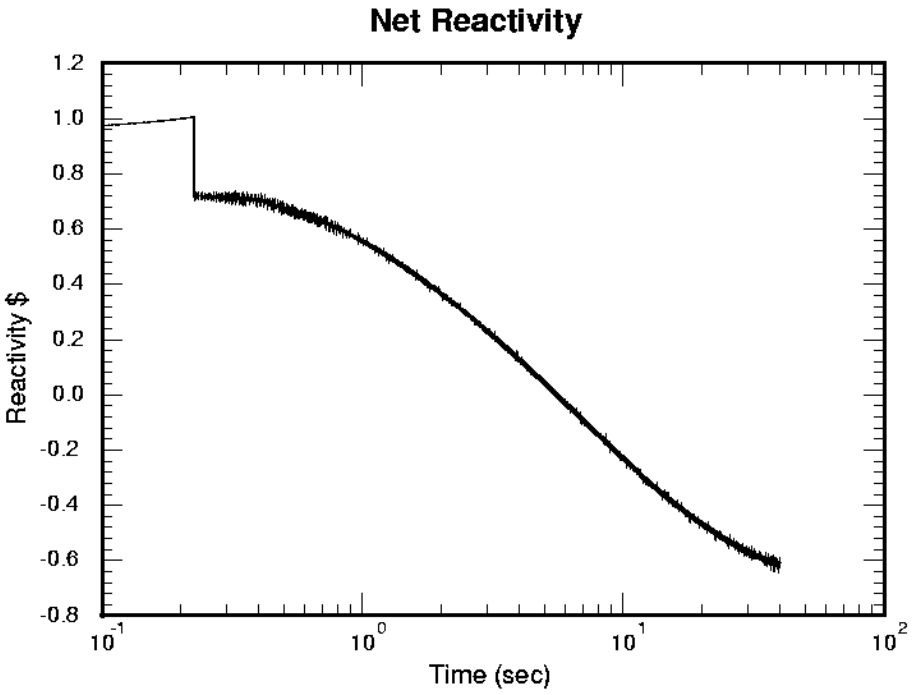

Figure 5.14. Reactivity of ZEDNA in a Worst Possible Accident Scenario

The predicted reactivity is less than zero at approximately 6 seconds. However, sufficient power decay remains in the core to cause significant additional heating, possibly melting the core.

Although the worst possible accident scenario may lead to melting of the core, it requires a rather extreme hardware failure, which is failure to drop the safety block.

6 Conclusions

A dynamic reactor model has been developed and applied to SPR-III and ZEDNA reactors. The dynamic reactor model includes the effect of transient core expansion and mass inertia for predicting reactivity feedback. For SPR-III, comparisons were made to actual measured pulses and to published data. In all cases the comparisons were good, with higher power pulses comparing more favorably than low power pulses. The dynamic reactor model was used to predict the performance of a ZEDNA reactor in both normal and off-normal conditions. The model predicts that the current conceptual ZEDNA reactor is quite robust and will not have any significant temperature excursions. Only an extreme case, where the reactor cannot be turned off, is fuel melting predicted to occur.

7 References

Biffle, J.H. (1987), "JAC3DA Three-Dimensional Finite Element Computer Program for the Nonlinear Quasi-Static Response of Solids with the Conjugate Gradient Method," SAND87-1305, Sandia National Laboratories, Albuquerque, NM, 1987.

Burgreen, D. (1962), "Thermoelastic Dynamics of Rods, Thin Shells, and Solid Spheres," *Nucl. Sci. Eng.* **12**, 203, 1962.

Eriksson, M., Cahalan, J. E., Wang, W. S. (2005), "On the Performance of Point Kinetics for the Analysis of Accelerator Driven Systems," *Nuclear Science and Engineering*, **149**, 298**,** 2005.

Hetrick, D. L. (1971), *Dynamics of Nuclear Reactors*, The University of Chicago Press, Chicago, IL, 1971.

Hoge, K.G. (1965), "Some Mechanical Properties of Uranium-10 wt Percent Molybdenum Alloy Under Dynamic Tension Loads. Proc. ASME Metals Engineering and Production Engineering Conference, Berkley, California, ASME 65-MET-8.

MCNP–A General Monte Carlo N-Particle Transport Code, Version 5, X-5 Monte Carlo Team, Diagnostics Applications Group, Los Alamos National Laboratory.

Miller, J. (1994), "Thermomechanical Analysis of Fast Burst Reactors," SAND94-0761C, Sandia National Laboratories, Albuquerque, NM, 1994.

Parma et. al. (2007), "An Externally Driven Neutron Multiplier Assembly Concept Using a Z-Pinch 14 MeV Neutron Source (ZEDNA)," SAND2007, January 2007.

Reuscher, J. A. (1969), "Thermomechanical Analysis of Fast Burst Reactors," Proceedings National Topical Meeting on Fast Burst Reactors, Albuquerque, NM, pp. 51-74, January 28–29, 1969.

Reuscher, J. A. (1972), "Analysis of Internal Heating Shock Effects in Reactor Fuel Components," *Nuclear Engineering and Design*, **18**, 213, 1972.

SPRF SAR (2005), "Safety Analysis Report (SAR) for the Sandia Pulsed Reactor Facility (SPRF)," SAND2005-4187, Sandia National Laboratories, Albuquerque, NM, 2005.

Wilson, S. C. and Biegalski, S. R. (2005), "An Iterative Method for Simulation of Dynamic Behavior in Fast Burst Reactors," *Transactions of the American Nuclear Society*, **93**, 590, 2005.

Wright, S.A. (2006), Personal Communication, April 2006.

Distribution:

1	MS1136	Curtis Peters, 6221
1	MS1136	Tom Lewis, 6221
1	MS1136	Tom Conboy, 6221
10	MS1136	Edward Parma, 1384
1	MS1141	Jim Dahl, 1383
1	MS1141	Dick Coats, 1383
1	MS1141	Paul Helmick, 1385
1	MS1141	Patrick Snouffer, 1385
1	MS1146	Jamie Cash, 1384
1	MS1146	Wu-Ching Cheng, 1384
1	MS1146	Phillip Cooper, 1384
1	MS1146	Russell DePriest, 1384
1	MS1146	Patrick Griffin, 2200
1	MS1146	Gary Harms, 1384
1	MS1146	Brian Hehr, 1384
1	MS1146	Don King, 1384
1	MS1146	Mike Luker, 1384
1	MS1146	Ken Reil, 1384
1	MS1146	Ahti Suo-Anttila, 1384
1	MS1159	James Bryson, 1344
1	MS0899	RIM-Reports Management, 9532 (electronic copy)


Sandia National Laboratories